Properties of the Nili Fossae Olivine-rich lithology: orbital and in situ at Séítah

Adrian Jon Brown[1], Linda C Kah[2], Lucia Mandon[3], Roger C. Wiens[4], Patrick C. Pinet[5], Elise Clavé[6], Stephane Le Mouelic[7], Arya Udry[8], Patrick J Gasda[9], Clément Royer[4], Keyron Hickman-Lewis[10], Agnès Cousin[11], Justin I. Simon[12], Jade Comellas[13], Edward Cloutis[14], Thierry Fouchet[15], Alberto Fairen[16], Stephanie Connell[4], David Timothy Flannery[17], Briony Heather Noelle Horgan[4], Lisa Mayhew[18], Allan H. Treiman[19], Jorge I. Núñez[20], Brittan Valhalla Wogsland[21], Karim Benzerara[22], Hans E. F. Amundsen[23], Kevin Peter Hand[24], Vinciane Debaille[25], Ari Essunfeld[26], Pierre Beck[27], Nicholas James Tosca[28], Juan Manuel Madariaga[29], and Olivier Forni[30]

[1]Plancius Research
[2]University of Tennessee at Knoxville
[3]California Institute of Technology
[4]Purdue University
[5]Univ. de Toulouse / CNRS
[6]University of Bordeaux
[7]LPGN
[8]Department of Geoscience, University of Nevada, Las Vegas
[9]Los Alamos National Laboratory (DOE)
[10]The Natural History Museum
[11]Institut de Recherche en Astrophysique et Planétologie - IRAP
[12]Center for Isotope Cosmochemistry and Geochronology, Astromaterials Research and Exploration Science, NASA Johnson Space Center
[13]University of Hawai'i at Mānoa
[14]University of Winnepeg
[15]Observatoire de Paris
[16]Centro de Astrobiologia
[17]Science and Engineering Faculty, Queensland University of Technology
[18]University of Colorado Boulder
[19]Lunar and Planetary Institute
[20]Johns Hopkins University Applied Physics Laboratory
[21]University of Tennessee
[22]Institut de Minéralogie, Physique des Matériaux et Cosmochimie, CNRS
[23]Earth and Planetary Exploration Services
[24]Jet Propulsion Laboratory
[25]Université Libre de Bruxelles
[26]Los Alamos National Laboratory
[27]Institut de Planétologie et d'Astrophysique de Grenoble, Université Joseph Fourier, Grenoble, France

[28]University of Cambridge
[29]University of the Basque Country
[30]Institut de Recherche en Astrophysique et Planétologie (IRAP) - CNRS

November 9, 2023

Abstract

We have studied the properties of the Nili Fossae olivine lithology from orbital data and in situ by the Mars 2020 rover at the Séítah unit in Jezero crater. We used the geochemistry collected by the rover's instruments to calculate the viscosity and relative flow distance of the Séítah unit. Based on the low viscosity and distribution of the unit we postulate a ponded lava flow origin for the olivine rich unit at Séítah. We calculate an approximate depth for the cumulate layer of the lava pond based on the viscosity of the unit and model of Worster et al. (1993).

We show that the resolution of orbital data is inadequate to map the phyllosilicate 2.38 μm band and demonstrate that it can be supplemented by in situ data from Mars 2020 SuperCam Laser Induced Breakdown Spectroscopy (LIBS) and reflectance observations to show that the low Al phyllosilicate in the olivine cumulate in the Séítah formation is either talc, serpentine, hectorite, Fe/Mg smectite, saponite or stevensite.

We discuss two intertwining aspects of the history of the lithology: 1) the potential emplacement and properties of the cumulate layer within a ponded lava flow, using previously published models of ponded lava flows and lava lakes, and 2) the limited extent of post emplacement alteration, including phyllosilicate and carbonate alteration.

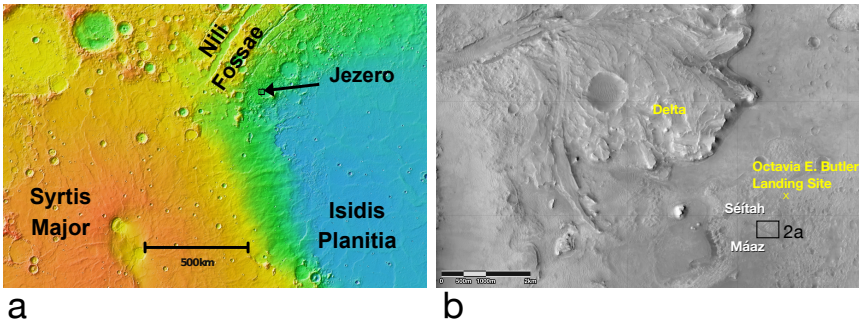

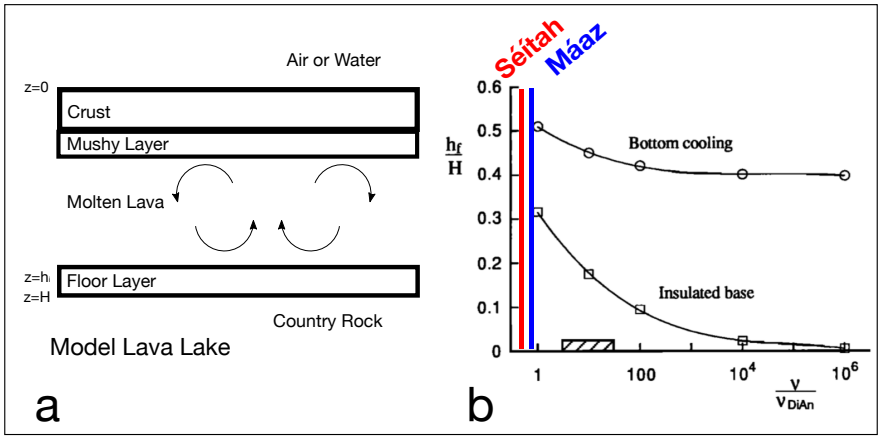

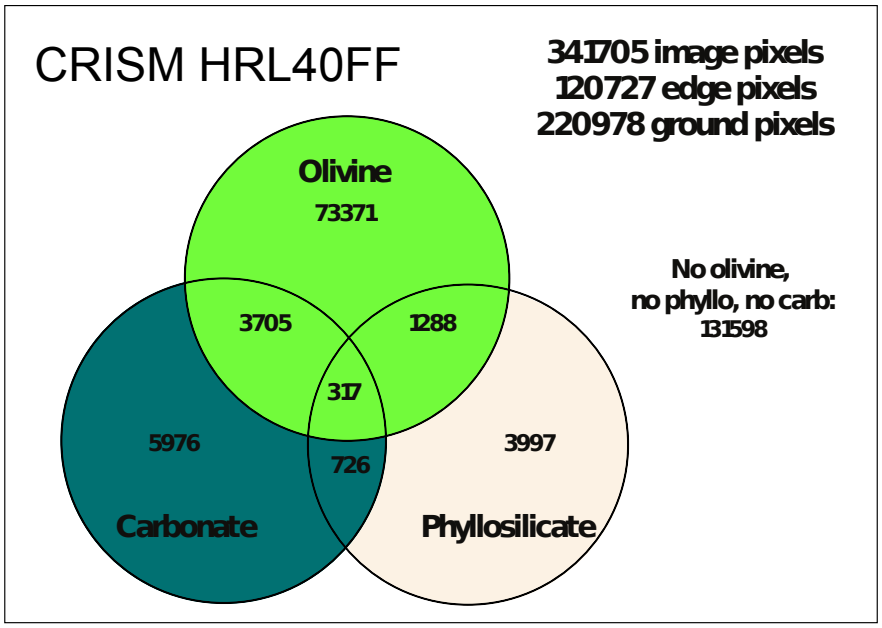

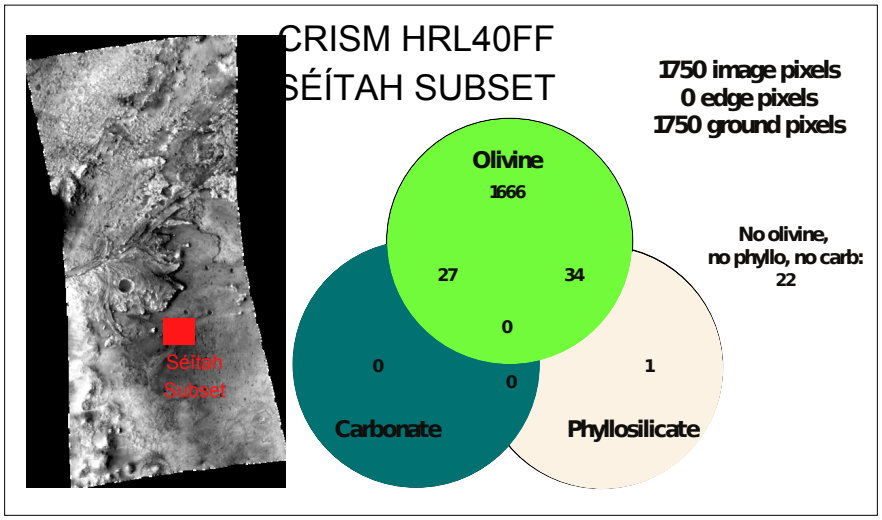

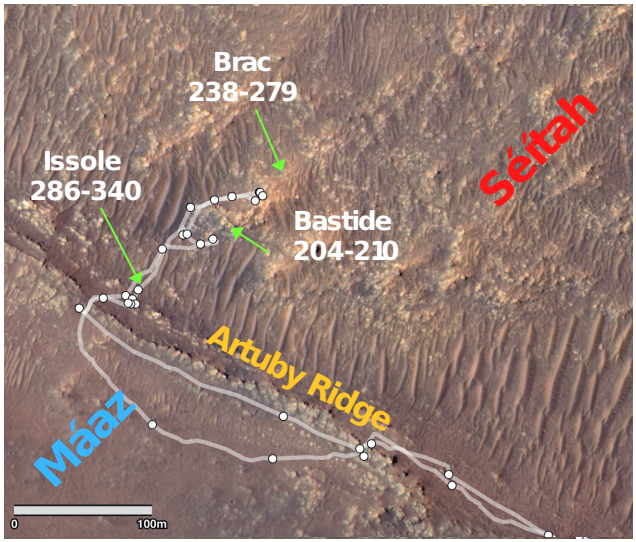
Brac
238-279
Séítah
Issole
286-340
Bastide
204-210
Artuby Ridge
Máaz
0
100m

a


Bastide Sol 204
Cine_206
Garde_207
Abrasion
PERSEVERANCE

b

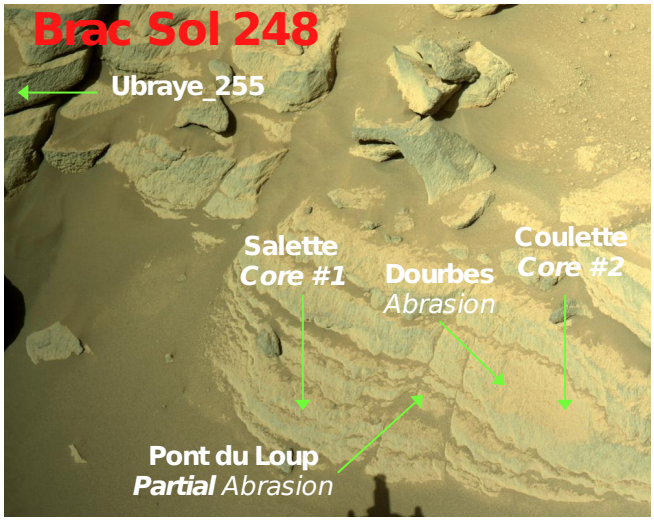
Brac Sol 248
Ubraye_255
Salette
Core #1
Dourbes
Abrasion
Coulette
Core #2
Pont du Loup
Partial Abrasion

c

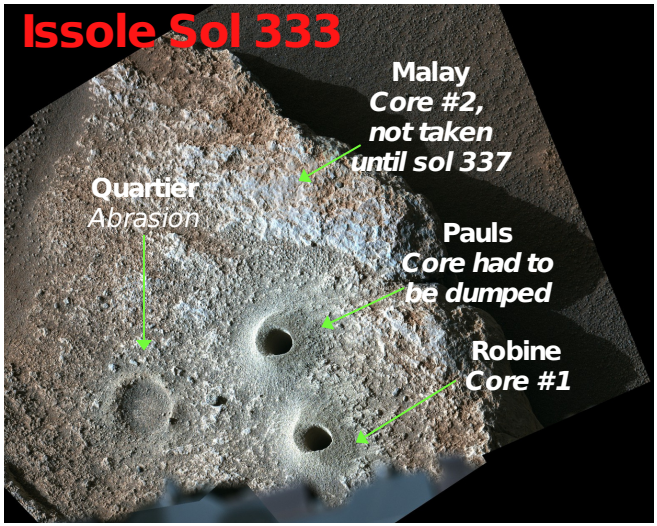
Issole Sol 333
Malay
Core #2,
not taken
until sol 337
Quartier
Abrasion
Pauls
Core had to
be dumped
Robine
Core #1

d

Properties of the Nili Fossae Olivine-rich lithology: orbital and in situ at Séítah

Adrian J. Brown*[1], Linda Kah[2] , Lucia Mandon[3], Roger C. Wiens[4], Patrick Pinet[5], Elise Clavé[6], Stéphane Le Mouélic[7], Arya Udry[8], Patrick J. Gasda[9], Clément Royer[10], Keyron Hickman-Lewis[11], Agnes Cousin[12], Justin I. Simon[13], Jade Comellas[14], Edward Cloutis[15], Thierry Fouchet[16], Alberto G. Fairén[17], Stephanie Connell[15], David Flannery[18], Briony Horgan[4], Lisa Mayhew[19], Allan Treiman[20], Jorge I. Núñez[21], Brittan Wogsland[2], Karim Benzerara[22], Hans E.F. Amundsen[23], Cathy Quantin-Nataf[24], Kevin P. Hand[25], Vinciane Debaille[26], Ari Essunfeld[9], Pierre Beck[27], Nicholas J. Tosca[28], Juan M. Madariaga[29], and Olivier Forni[12]

[1]Plancius Research, Severna Park, MD 21146. [2]Department of Earth and Planetary Sciences, University of Tennessee, Knoxville TN 37996, [3]Division of Geological and Planetary Sciences, California Institute of Technology, Pasadena, CA, [4]Earth, Atmospheric, and Planetary Sciences, Purdue University, [5]IRAP, Observatoire Midi-Pyrénées,CNRS, Toulouse university, France, [6]CELIA, Université de Bordeaux, CNRS, CEA, [7]Laboratoire Planétologie et Géosciences, CNRS UMR 6112, Nantes Université, Université Angers, 44322 Nantes, France, [8]Department of Geoscience, University of Nevada Las Vegas, 89154 Las Vegas, NV, [9]Los Alamos National Laboratory, PO Box 1663 Los Alamos, NM 87545, [10]LESIA, Observatoire de Paris, Université PSL, CNRS, Sorbonne Université, Université de Paris, Meudon, France, [11]The Natural History Museum, Cromwell Road, London, SW7 5BD, UK, [12]IRAP, Observatoire Midi-Pyrénées, CNRS, Toulouse university, France, [13]Center for Isotope Cosmochemistry and Geochronology, Astromaterials Research & Exploration Science Division, NASA Johnson Space Center, 2101 Nasa Parkway, Houston, TX, 77058 USA, [14]University of Hawai'i at Mānoa, [15]University of Winnipeg, Canada, [16]LESIA, Observatoire de Paris, Université PSL, CNRS, Sorbonne Université, Université de Paris, Meudon, France, [17]Centro de Astrobiologia (CSIC-INTA) & Cornell University, NY, [18]Queensland University of Technology, Queensland, Australia, [19]Department of Geological Sciences, University of Colorado Boulder, Boulder, CO 80309, [20]Lunar and Planetary Institute, Houston TX 77058, [21]Johns Hopkins University Applied Physics Laboratory, Laurel, MD 20723, [22]Institut de Minéralogie, Physique des Matériaux et Cosmochimie, CNRS, Museum National d'Histoire Naturelle, Sorbonne Université, Paris, France, [23]CENSSS, University of Oslo, Norway (Deceased), [24]University of Lyon, France, [25]Jet Propulsion Laboratory, Pasadena, CA 91109, [26]Laboratoire G-Time, Université libre de Bruxelles, Brussels, Belgium, [27]Institut de Planétologie et d'Astrophysique de Grenoble IPAG/CNRS, Université Grenoble Alpes, 414 rue de la piscine, 38041 Grenoble cedex 09, France, [28]Department of Earth Sciences, University of Cambridge, Downing Street, Cambridge, CB2 3EQ, United Kingdom, [29]Department of Analytical Chemistry, University of the Basque Country UPV/EHU, 48940 Leioa, Spain

Corresponding author: Adrian J. Brown **(adrian.j.brown@nasa.gov)**

Key Points:

- **We use orbital data and a Venn diagram analysis to show the Séítah olivine lithology remains largely unaltered**
- **We postulate a ponded lava flow origin for the Séítah formation based on finding low Al olivine cumulate with low viscosity**
- **We find the low Al phyllosilicate in the cumulate olivine at Séítah is talc, serpentine, hectorite, Fe/Mg smectite, saponite or stevensite**

Plain Language Summary

We used orbital and in situ data to observe a lava flow containing the mineral olivine near the Mars 2020 landing site at Jezero Crater. By analyzing the reflectance spectra of the rocks containing the lava, we have identified that clay is present in the olivine bearing rocks. We use in situ imaging data to determine that the lava contains the olivine in close packed crystals (cumulate), a process which can happen in the bottom of a lake of lava. We use measurements from the in situ rover instruments to determine that the cumulate is accompanied by clays.

Abstract

We have studied the properties of the Nili Fossae olivine lithology from orbital data and in situ by the Mars 2020 rover at the Séítah unit in Jezero crater. We used the geochemistry collected by the rover's instruments to calculate the viscosity and relative flow distance of the Séítah unit. Based on the low viscosity and distribution of the unit we postulate a ponded lava flow origin for the olivine rich unit at Séítah. We calculate an approximate depth for the cumulate layer of the lava pond based on the viscosity of the unit and model of Worster et al. (1993).

We show that the resolution of orbital data is inadequate to map the phyllosilicate 2.38 μm band and demonstrate that it can be supplemented by in situ data from Mars 2020 SuperCam Laser Induced Breakdown Spectroscopy (LIBS) and reflectance observations to show that the low Al phyllosilicate in the olivine cumulate in the Séítah formation is either talc, serpentine, hectorite, Fe/Mg smectite, saponite or stevensite.

We discuss two intertwining aspects of the history of the lithology: 1) the potential emplacement and properties of the cumulate layer within a ponded lava flow, using previously published models of ponded lava flows and lava lakes, and 2) the limited extent of post emplacement alteration, including phyllosilicate and carbonate alteration.

1. Introduction

1.1 Purpose of paper

This paper uses the latest findings of the Mars 2020 rover mission to infer the properties of the regional Nili Fossae olivine rich lithology, including composition (Liu et al., 2022 and Corpolongo et al., 2023) and grain size (Tice et al., 2022), and calculates a model viscosity, based on the geochemistry of Wiens et al., (2022). We also use orbital hyperspectral data alongside in situ SuperCam reflectance measurements to derive new knowledge regarding the accompanying phyllosilicates in the olivine cumulate at Séítah.

Importance of Viscosity. As we shall discuss further in this paper, viscosity is a key characteristic of a lava flow, determined by a variety of factors, including its composition, temperature, water, crystal content and pressure. The viscosity is a critical parameter for controlling the morphologic expression of the erupted unit. Critically, it allows us to compare the lava with other similar flows across Mars, and place it in context with the dominant rock-forming processes on terrestrial planets. The inferred viscosity has now become available from the first in situ measurements of the Jezero crater floor geochemistry.

Olivine rich lithology and relationship to Landing Site. The olivine rich lithology was discovered using telescopic observations by Pinet and Chevrel (1990). As seen in Figure 1, it was subsequently mapped to extend throughout the Nili Fossae region, and is associated with radial graben on the northwest side of the Isidis Basin (Kremer et al., 2019). The landing site of the Mars 2020 rover was chosen to be at Jezero Crater, the site of a delta deposit which indicated the crater previously was filled with liquid water (Fassett and Head, 2005). The rover landed on Feb 18, 2021, to the southeast of the delta (Sun et al., 2023). Around 200 sols (Martian days) later, the rover traversed around the edge of the Séítah region (Figure 1b), which is covered in linear dunes that were deemed to be too difficult to traverse. The delta was determined from orbit to have a similar spectral signature to the olivine lithology mapped outside the crater (Goudge et al., 2015).

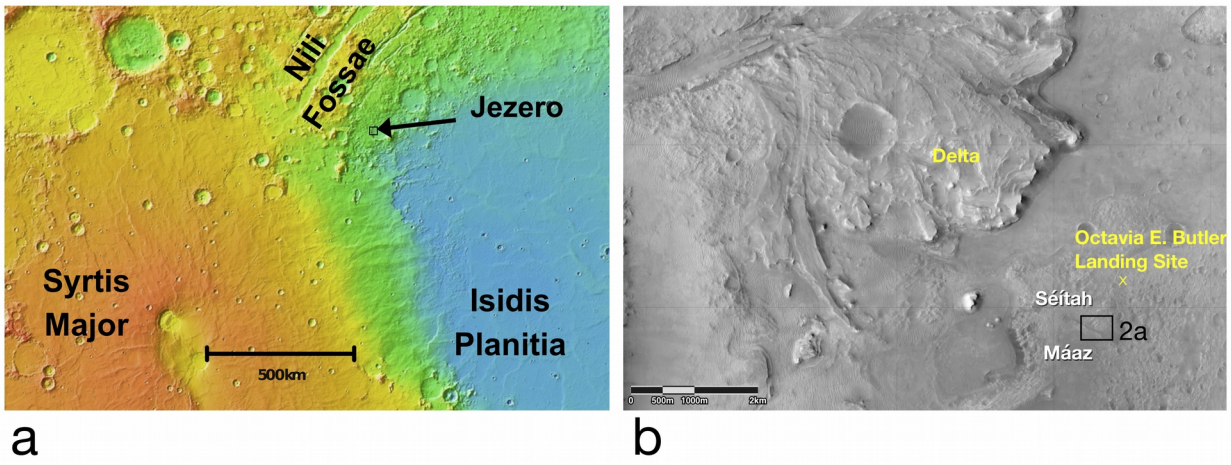

Figure 1. a. MOLA image showing the relationship of western edge of the Isidis Basin complex, giving the relative positions of Syrtis Major, Nili Fossae and Jezero Crater. b. HiRISE map of Jezero Crater showing the delta and Octavia E. Butler landing site and Séítah and Máaz Formations and location of Figure 2a.

Previously the lithology has been known to be olivine-bearing (Hoefen et al., 2003; Tornabene et al., 2008) or olivine-carbonate (Ehlmann et al., 2008; Mandon et al., 2020; Brown et al., 2020), however, this paper is designed to quantitatively analyze the relationship between olivine, carbonate and phyllosilicate and investigate, using a Venn diagrammatic approach, the suggestion that where there is carbonate, there is also clay (Horgan et al., 2020; Tarnas et al., 2021).

We address in detail two aspects of the Séítah lithologic history: 1.) the emplacement of the cumulate layer within a ponded lava flow, based on previously published models of lava ponding in lakes (Worster et al., 1993), and 2.) the limited extent of post emplacement alteration, including phyllosilicate and carbonate alteration of the Séítah formation (Clavé et al., 2023; Mandon et al., 2023). These aspects of the history of the Séítah unit demonstrate that observations and models are both needed to uncover further insights into the emplacement and subsequent alteration history of this important Martian lithology, which has now been sampled for return to Earth (Simon et al., 2023).

Unit Interpretations. Farley et al. (2022) provide interpretations for the rock lithologies discussed in this paper. Farley et al. described the Séítah (an olivine cumulate) and Máaz (a pyroxene- and plagioclase-dominated unit overlying Séítah) formations that were encountered and mapped during the Crater Floor campaign in the first 380 sols of the Mars 2020 mission. We discuss interpretations arising from the Séítah formation, which has previously been interpreted as related

to the olivine-carbonate lithology inside and outside Jezero (Goudge et al., 2015, Brown et al., 2020). Figure 2 presents a visual summary of the traverse through the Séítah formation and the three key workspaces, and all the targets referred to in this paper. Farley et al. (2022) further described the Artuby member which runs along a eponymous ridge between the Máaz and Séítah formations (Figure 2a).

Relevant Workspaces. On Sol 202 of the mission the rover rolled into the Séítah formation, and approached the Bastide workspace (a location where the rover analysed several rock surfaces). For the purposes of this study, we identify three main workspaces - in temporal order, Bastide, Brac and Issole. These workspaces and the abrasions and samples taken at each workspace are also shown in Figure 2. The rover left Séítah on Sol 340. See also (Sun et al., 2023; Crumpler et al., 2023; Beyssac et al., 2023) for more details on the Crater Floor campaign and stratigraphic information obtained during the Séítah traverse.

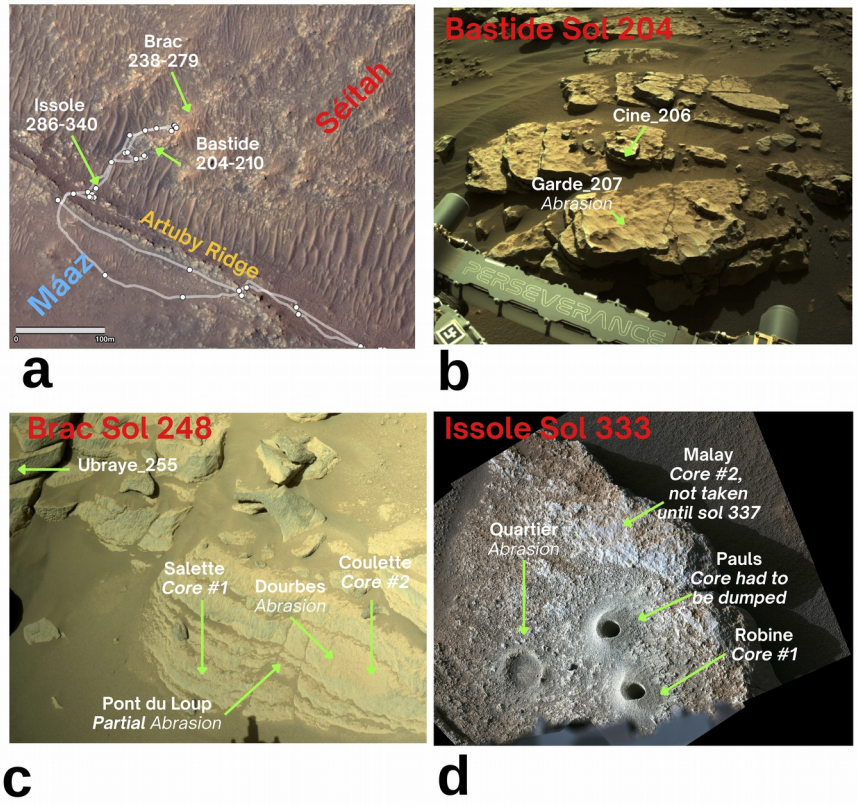

Figure 2. a.) HiRISE overview map of the Séítah traverse showing the three key workspaces: Bastide, Brac, and Issole, and the Sol counts at each. b.) Navcam image of Bastide Workspace taken on Sol 204. c.) Navcam image of Brac Workspace on Sol 248, before samples were taken d.) Mastcam-Z image of Issole on Sol 333 after Robine and Pauls samples and Quartier abrasion were taken but before sample Malay was obtained.

Definition of phyllosilicate. Due to its importance in this paper, we first establish a clear and distinct definition of the word "phyllosilicate". Here by "phyllosilicate" we are referring to the mineral group of phyllo-silicates ("φύλλο" in Greek is "leaf" in English). These layer-silicates have stacked hydroxyl (-OH), octahedral (O) sheets and tetrahedral (T) silicate (Bailey, 1988). The octahedral sheets come in two forms called dioctahedral and trioctahedral which host divalent (Fe^{2+}/Mg^{2+}) and trivalent (e.g., Al^{3+}/Fe^{3+}) cations respectively. Phyllosilicates come in many families, based on the stacking of layers (e.g. TO or 1:1 vs TOTTOT or 2:1). In this paper we are particularly interested in the 2:1 phyllosilicates talc and 1:1 serpentine and the 2:1 phyllosilicate family called smectites.

1.2 Previous work

1.2.1 Infrared remote observations

The Syrtis Major shield region was first observed to host a distinct mafic unit using Visible and Near InfraRed (VNIR) telescopic observations by Pinet and Chevrel (1990). Spacecraft observations followed, and a decade later the Thermal Emission Spectrometer (TES) infrared (IR) instrument on Mars Global Surveyor also recognised a strong 10 μm absorption band associated with the Nili Fossae region that was attributed to olivine (Hoefen et al., 2003; Hamilton and Christensen, 2005). The Observatoire pour la Minéralogie, l'Eau, le Glace et l' Activité (OMEGA) instrument on Mars Express was able to determine that phyllosilicates were also associated with the olivine, suggesting Fe-rich smectites were present (Mustard et al., 2007; Mangold et al., 2007). Using data from the Compact Reconnaissance Imaging Spectrometer for Mars (CRISM) instrument, Mg-carbonate was discovered to be associated with the olivine lithology by using the strength and position of the 2.3 and 2.5 μm bands (Ehlmann et al., 2008). The olivine-carbonate was hypothesized to be due to serpentinization by Brown et al. (2010), who also suggested that talc might be present by analogy to talc-carbonate terrestrial Archean greenstone terranes. Brown et al. (2010) also found the carbonate to be a 50/50 Fe/Mg mixture, which was later supported using TES orbital data analyzed by Ruff et al. (2022). Goudge et al. (2015) mapped the watershed of the Jezero deltas and the accompanying mineralogy. Mafic minerals and Margin Carbonates were identified in the mapping study of Horgan et al. (2020). Mandon et al. (2020) used OMEGA observations to map the olivine and carbonate, and used crater counting and stratigraphic relationships to date the unit at ~3.82 Ga. The olivine composition (Fo#44-66) and grain size (~ 1mm) were first estimated to be millimetric by Poulet et al (2009) using OMEGA observations, and later modeled by Edwards and Ehlmann (2015) and by Brown et al. (2020) using

CRISM data.

A recent map of the mineralogy of Jezero crater using CRISM data illustrates the locations of multiple minerals and mineral combinations including olivine, Mg-rich carbonate, olivine+Fe/Mg-smectite, high-Ca pyroxene, and low-Ca pyroxene (Parente et al., 2021). This map was created using a new algorithm for atmospheric correction (Itoh and Parente, 2021) that enhances the spectral features due to surface outcrops and an improved mapping procedure (Saranthan and Parente, 2021).

Finally, a recent closely related study of VNIR spectra of phyllosilicates in the Archean Barberton Greenstone Belt has identified serpentine and chlorite after olivine and suggested that the phyllosilicates were formed by hydrothermal alteration (Grosch et al., 2021).

1.2.2 SuperCam LIBS observations

SuperCam is a multi-technique instrument suite mounted on the Mars 2020 *Perseverance* rover (Wiens et al., 2021; Maurice et al., 2021). It is an upgraded version of the ChemCam instrument onboard the Mars Science Laboratory (MSL) *Curiosity* rover. It has the capability to obtain LIBS measurements to a distance of ~10 m, and to quantify the major element abundances at distances up to 6.5 m. The Remote Micro-Imager (RMI) is a color telescope used to provide context images for SuperCam observations.

The SuperCam instrument has been used to investigate the igneous nature of the Séítah and Máaz regions, as reported by Wiens et al. (2022), Beyssac et al. and Udry et al. (2023). These studies concentrated on chemistry and mineralogy, and creation of a stratigraphy of the two regions of the Jezero crater floor. In this paper we use LIBS elemental abundances for the Séítah and Máaz formations reported in the Wiens et al. (2022) study.

1.2.3 SuperCam VISIR observations

SuperCam VISIR is an optical spectrometer that covers the 0.4-0.85 and 1.3-2.6 µm wavelength ranges, providing reflectance spectra boresighted with the LIBS and RMI instruments (Weins et al. 2021; Maurice et al. 2021; Fouchet et al., 2022). This paper relies on the calibration and comparison of the spectra presented here with others measured by the rover in situ. Royer et al. (2023) shows that, based on band depth calculations and noise estimates, that most of the 2.46 µm detections we will discuss herein range from Signal to Noise Ratio (SNR) = 4 to SNR = 12. This spectral range near 2.46 µm is harder to study because of the fact that many

spectral signatures are sampled with the minimum sampling (at most 2 spectral channels in the band) and several artifacts may be similar to absorption features (e.g., non-corrected spikes, calibration residuals). In our case, regarding the 2.46 μm region, we have SNR > 5 and as demonstrated below, detections of small bands in this region are realistic, given the accuracy of the calibration and the potential residuals. Positive detections must nevertheless be confirmed visually and their attribution validated by the presence of other features characteristic of phyllosilicates.

Mandon et al. (2023) reported the spectral properties of the rocks of the crater floor as measured by the VISIR on SuperCam, and they were able to recognize widespread but low intensity alteration mineralogy. They assigned the alteration into two phases containing phyllosilicates and oxyhydroxides, and then later sulfates. They interpreted these as happening under lake or deeper serpentinization conditions and later evaporative environments.

SuperCam's VISIR data allow on-ground comparison with absorption features seen from orbit by the CRISM instrument. Due to the fact that CRISM covers a larger spectral range (0.4-3.96 μm), in this paper we adopt a band fitting comparison strategy over the 1.3 to 2.5 μm range.

1.2.4 PIXL observations

The Planetary Instrument for X-ray Lithochemistry (PIXL) is a high resolution X-Ray fluorescence microscope in situ scanning instrument mounted on the arm turret of the rover (Allwood et al., 2020). PIXL observations of the Séítah formation have been used to identify the cumulate nature of the target and infer an igneous origin (Liu et al., 2022). The olivine composition is consistently homogeneous, and of Fo55+/-1 within a several mm analysis patch (Liu et al., 2022), which is a reasonable match with previous orbital work constraining the Nili Fossae olivine Fo# to 44-66 (Brown et al., 2020). PIXL's X-ray diffraction capability, which can identify coherent crystalline domains, has been used to identify coarsely grained (1-2 mm), interlocking olivine grains (Tice et al., 2022), and SuperCam's RMI instrument measured a mean grain size of 1.45+/-0.20 mm over the rover's Séítah formation traverse (Wiens et al. 2022). These in situ observations are both good matches for the ~1 mm Nili Fossae olivine grain size calculation from orbital studies prior to landing (Brown et al., 2020).

2. Methods

2.1 Viscosity calculations

2.1.1 Giordano empirical melt viscosity model

In order to calculate the inferred melt viscosity of the samples treated in this study, we have used the empirical approach of Giordano et al. (2008), which calculates a viscosity vs. temperature curve for a magmatic silicate liquid. Their method uses a single equation with 17 parameters and the temperature of the melt . They then use this equation to calculate the contributions of the elemental oxides common to terrestrial magma bodies to arrive at an inferred viscosity for a magma of that composition.

We have used the SuperCam LIBS geochemical elemental abundances for the Máaz formation, Artuby member and Séítah formation from Wiens et al. (2022). Wiens et al. (2022) made a partial correction for the LIBS compositions by removing all data points that were float rocks, soils, and apparent coatings, as well as all points that had major-element totals < 80 wt%. The latter step removes a large number of points with alteration, especially anything that included significant sulfate or carbonate contributions. Wiens et al. (2022) investigated how the removal of points affected the bulk compositions, and determined that the 80 wt% was a reasonable limit. In this study, we have made no further attempt to petrologically correct the measured bulk compositions to the original magma, and will instead pursue this approach in future work.

We have chosen to use the SuperCam LIBS results over the PIXL measurements, which were obtained from points on the scale of microns, because we believe the SuperCam averages will be better representatives of the average of the units on the scale of the lithology for the comparison with orbital data.

2.1.2 Previous Martian lava flow models

Martian gravity is ~37.5 % of that on Earth. At the time of emplacement of the Séítah formation, the Noachian atmosphere was likely thicker that it is presently, however it is challenging to constrain this aspect of Martian history. Following other lava flow model studies (e.g. Rowland et al. 2004), and assuming Mars possessed a thinner (~6 mbar) atmosphere throughout its history, we can compare terrestrial lava properties to those of Mars (Wilson and Head, 1994). On Mars, with a thinner atmosphere, lava will take longer to cool. Longer cooling periods

should also drive larger crystal growth. Wilson and Head (1994) predicted Martian volcanic flows (driven by lower gravity) to be longer than compositionally identical flows on Earth, leading to spatially larger deposits on the smaller planet. However it was later established by Rowland et al. (2004) using a more rigorous lava cooling model called FLOWGO that lower Martian gravity actually leads to shorter lava flows. They showed that all other factors being equal, a lower value of g will result in a lower velocity of flow by 3.7/9.8 (~60%), which leads to shorter Martian lava flows by almost half, all other conditions being held constant.

2.1.3. FLOWGO Model.

After lavas erupt from a vent or fissure, they will cool as they flow across a planetary surface. The FLOWGO program is designed to model this process and tracks the evolving flow velocity, temperature and viscosity of the cooling lava for a designated lava eruption effusion rate, composition, planetary atmosphere, local slope and gravity field (Harris and Rowland 2001). For this project, we used the PyFLOWGO code, which is available in Python on GitHub (Chevrel et al., 2018). FLOWGO can be used to calculate the run out distance away from the lava vent based on the surface stress stopping condition, as the lava cools to a temperature which prevents forward movement. FLOWGO has been used previously to model lava flows in the Martian enironment (Rowland et al., 2004).

The cooling equation for FLOWGO is based on Jeffrey's equation (Jeffreys 1925):

$$u=\rho_{lava} g.\sin(\alpha) d^2/\nu \quad (1a)$$

which is a solution for the incompressible, steady flow form of the Navier-Stokes equation in a uniform channel (Jeffreys, 1925):

$$du/dt = g.\sin(\alpha) + \nu d^2u/dz^2 \quad (1b)$$

u is the velocity of the flow, ρ_{lava} is the density of the lava, g is the gravitational constant, α is the local slope, d is the channel depth and ν is the kinimatic viscosity of the fluid.

Inherent limitations of FLOWGO. The Jeffreys equation is valid for purely viscous non-turbulent flows where the channel is of uniform width. The channel slope is assumed known ahead of time in order to complete the calculation. The planetary

atmosphere and composition is assumed to remain invariant during the calculation.

Cooling and Volume-limited flows. Finally, it should be noted that the FLOWGO model is appropriate only in the case of "cooling-limited" flows, where the lava flow halts as it cools (Guest et al., 1987). If the lava flow is halted due to a magma cut off, the flow will be "volume-limited" and much shorter than calculated using equation (1).

Discharge rate. The Reynolds number of a liquid flow can be calculated as (Huppert et al., 1984):

$$R_e = E/\nu \qquad (2)$$

Here E is the discharge rate and v is the kinematic viscosity. R_e is a threshold for turbulence, the critical value is typically ~2000.

At high Reynolds number, the discharge rate E of lava through a long fissure of width d can be calculated thus:

$$E = d^{3/2}(g\Delta\rho)^{1/2}/(k\rho)^{1/2} \qquad (3)$$

Here k is a friction coefficient, $\Delta\rho$ is the density difference between the magma and lithosphere, and ρ is the magma density.

2.1.4 Lava ponding and cumulate formation models

Since the studies of Shaw (1965) and Bartlett (1965), it has been recognized that convection is an important part of the cooling process of magma bodies and lava lakes. Convection is higher in low viscosity melts. For crystals to form in a cooling body, the temperature contrast must drop below the liquidus temperature of the melt. Without convection, this would occur only at the interface between crystals and the surrounding melt. Brandeis and Marsh (1989) suggested that this would lead to limited convection in magma chambers. However, Worster et al. (1990) were able to show that in fact crystallization is extended to the interior of the magma or lava pond by convection, and also showed this process allows crystals to form at the base of the chamber even when it is cooled from the roof.

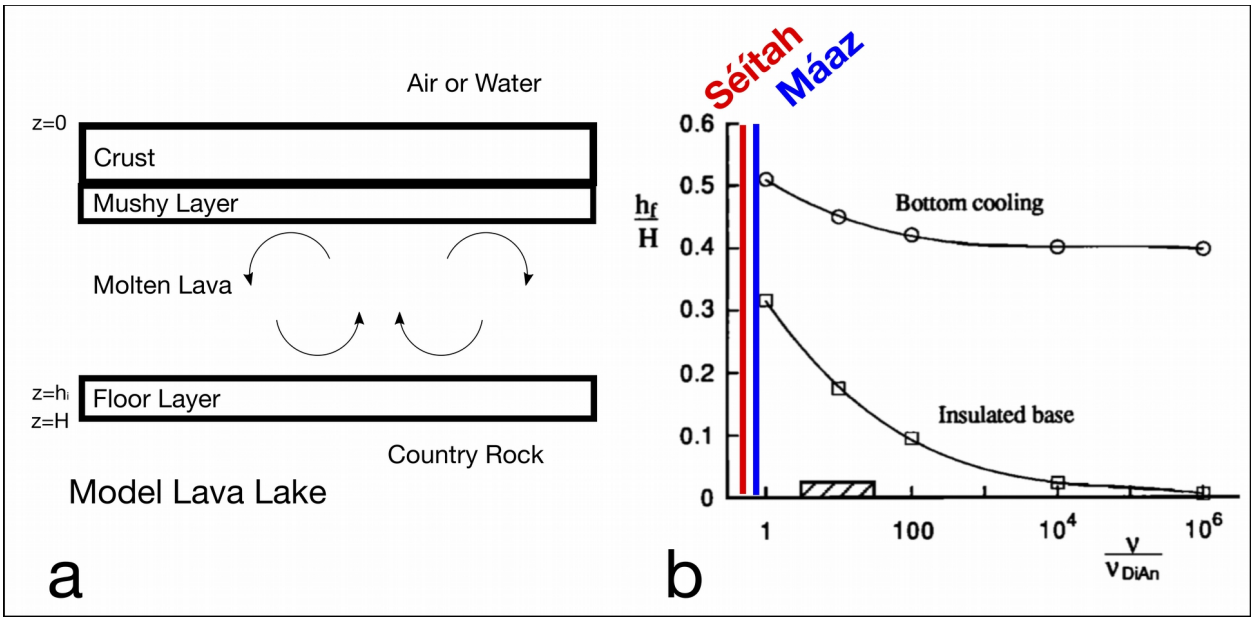

Figure 3. a.) Thermal model of a lava lake with layers representing solid crust/cap, mushy layer (where crystals form), molten lava (with convection taking place) and the floor. b.) Final fractional height of floor layer, h_f, where crystals accumulate (relative to the height of the chamber height, H) plotted against the lava viscosity (normalized relative to liquid diopside-anorthite). Two cases are shown, one in which bottom cooling occurs, and one in which it does not (insulated base). The dashed box indicates the viscosity of typical terrestrial basalt relative to a pure diopside-anorthite melt, after Worster et al. (1993). The Séítah and Máaz viscosities calculated in this paper are schematically shown on the plot.

Development of cumulate texture. The large grain size (Tice et al., 2022) and cumulate texture (Liu et al., 2022; Tice et al., 2022) initially lead us to explore the possibility of the Séítah rocks being emplaced as a Martian lava lake. Worster et al. (1993) developed a thermodynamic model for a terrestrial lava lake, and outlined how the body would form compositional and textural layers within the resultant rock as it cooled. They showed that a lava lake can develop quickly when a lava flow fills a topographical depression, and showed that convective cooling can take place. They examined the situation with and without convection in their model and found thermal convection drives internal crystallization within the melt. This in turn forms layering at the floor of the lake as crystals fall out of suspension. Cooling by thermal conduction alone does not produce this layering. Figure 3a shows a schematic diagram of an idealized lava lake after Worster et al. (1993). For this study, we are interested in lava lakes that convect and develop internal stratification (i.e. layering) as shown in this diagram.

Effect of viscosity. Figure 3b shows the effect of viscosity on the cooling history of a lava lake that is cooled from the top. This figure shows the major effect of viscosity on lava lake crystallization, as studied by Worster et al. (1993). The parameter h_f is the final floor layer (Figure 3a) depth, and H is the total depth of the

lava lake. It can be seen that the relative size of the floor layer grows with decreasing viscosity, and this effect is more pronounced when the bottom of the rock is insulated. We show schematically with vertical lines where the Séítah and Máaz units viscosity would plot (relative to liquid diopside-anorthite, DiAn), indicating that Séítah-like viscosities would produce a deeper cumulate floor layer than a Máaz-like viscosity. The equation for the calculation of the viscosity of diopside-anorthite adopted by Worster et al. (1993) (their Table 2) is:

$$\nu = \exp[12\text{-}52.5x\text{+}62.5x^2]\ln(10)] \quad (4)$$

where $x = 1\text{-}1000/(T\text{+}273)$ and

T is the temperature of the melt in degrees C.

The takeaway message from this section is that lower viscosity lavas build thicker cumulate layers. We shall use this model to enhance the interpretations of our in situ observations later in this study.

2.2 Phyllosilicate alteration mineralogy

We will now discuss the methods used in this paper to analyse visible to near infrared (SWIR, 1.0-2.5 μm) reflectance spectra to identify and map phyllosilicates using asymmetric band fitting, and give a short introduction to the chemical formulas of the phyllosilicates that we are interested in for this study.

We have used a single image cube of CRISM data from the Map Projected Targeted Data Record (MRTDR) calibration standard, as described by Seelos et al. (2012). This processing level removes most atmospheric effects and presents each pixel in apparent reflectance space, which is suitable for comparison with spectral library spectra or SuperCam VISIR processed spectra.

2.2.1 CRISM and VISIR phyllosilicate identification

Figure 4 shows library spectra of talc, lizardite, stevensite, Fe/Mg smectite, hectorite and saponite in the VIS and SWIR (Short Wave InfraRed) regions, which are covered by the SuperCam VISIR instrument. The talc and lizardite spectra are sourced from the USGS Spectral Library (Clark et al 2007). The stevensite specimen was provided by Nicholas Tosca and measured at the University of Winnipeg Planetary Spectrophotometer Facility. Hectorite SHCa-1 (JB0172, <2 μm) and saponite SapCa-1 (JB1184c, 125-150 μm) were obtained from the Clay Minerals Source Clays Repository and the Fe/Mg smectite sample (JB0761a, <125

μm) was collected by J. Post from Flagstaff Hill, CA. Spectra of the hectorite and Fe/Mg smectite samples are described in Bishop et al. (2008a), while the saponite spectra are described in Roush et al. (2015). Further information on sample provenance is provided in supplemental section S2.

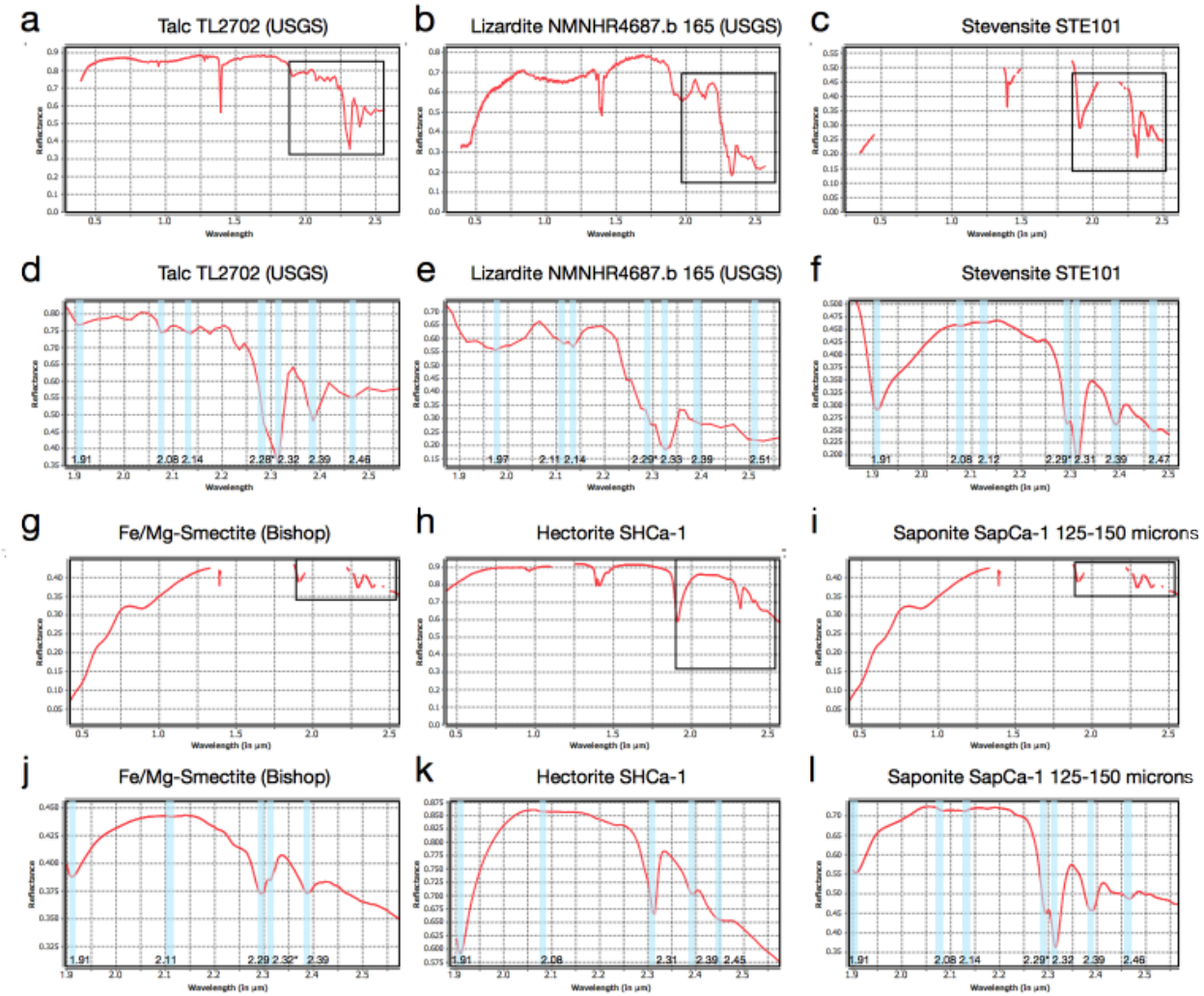

Figure 4. Laboratory spectra of a.,d.) Talc b.,e.) Lizardite c.,f.) Stevensite g.,j.) Fe/Mg-smectite (Bishop) h,k.) Hectorite SHCa-1, i,l.) Saponite SapCa-1. Shown at top is the visible and SWIR region of the spectrum, on the bottom is a zoom into the SWIR region at the location shown in the box on the upper spectra. Note: 1) strength of 2.31 μm band in talc and 2) the presence of a weak 2.46 μm band in talc which is not present in lizardite.

The SWIR absorption bands of the Fe-bearing phyllosilicates nontronite (Bishop et al., 2013) and hisingerite (Turrenne et al., 2023) both display strong 2.28 μm bands which are not present in the spectra of olivine bearing targets we report here, so they are not considered further.

Mandon et al. (2023) reported seeing 2.28 μm bands in the "pitted" outcrops of Séítah and Máaz (which were largely olivine-free), however the band was relatively shallow and only present at greater than 3% absorption band depth in less than 5% of the spectra in dark toned rocks. These bands are even weaker with the Séítah olivine-bearing cumulate rocks seen by Mandon et al. (2023), and we consider that consistent with our findings here.

The key bands of the spectra are noted in the plot, and we draw the reader's attention to the relative strength of the 2.31 (strong), 2.38 (moderate to weak) and 2.46 μm (weak) bands in particular. The other two spectral differences for the purpose of this paper are 1) the strength of the 2.38 μm band, which is weak in the serpentine lizardite (Figure 4e), but far stronger in the other phyllosilicates in Figure 4, and 2) the presence of a weak 2.46 μm band in talc (Figure 4e) which is only a shoulder (at most) in lizardite (Figure 4e). These spectral differences will be discussed later in the paper.

2.2.1.2 Band fitting with an Asymmetric Gaussian shape

As has been previously discussed in Brown (2006a), the natural bandshape for an absorption band in energy space is a Gaussian shape. When accompanied by nearby and often closely related bands, for example, due to Tschermak substitution of Mg^{2+} and Fe^{2+} (Duke, 1994), the vibration bands can adopt an asymmetric shape. It is then advantageous to carry out an asymmetric band fit. Figure 4 demonstrates that all three of the phyllosilicate related bands are asymmetric and extend to the left (higher energy). As part of this fitting process we obtain four parameters per band: the amplitude, width, centroid (position), and the asymmetry (Brown et al., 2010). We primarily use the amplitude band parameter, and cross-correlate the amplitude of the olivine 1 μm band, 2.31 μm (phyllosilicate or carbonates), 2.5 μm (mostly carbonate, however there is a weak serpentine 2.5 μm band (Figure 4f)), and 2.38 μm (phyllosilicate only) band amplitude maps.

2.2.2 Ideal Chemical formulas of serpentine, talc and smectites

*Smectites***.** Dioctahedral smectites contain two cations with a charge of 3+ (typically Al^{3+} or Fe^{3+}) in their octahedral sheets (for example montmorillonite and nontronite), while trioctahedral smectites contain three cations with a charge of 2+ (typically Mg^{2+} and sometimes Fe^{2+} or other transition metals) with the Mg-rich form called hectorite, stevensite, or saponite, where saponite has tetrahedral substitution and hectorite does not. Stevensite has additional charge due to cation vacancies in the octahedral sheets.

Beidelite and saponite are special cases of smectites where Al^{3+} substitutes for Si^{4+} in the tetrahedral sheets, causing a disruption of the structure and creating surface charge. Stevensite and hectorite do not typically contain any Al^{3+} cations. We note that the Fe/Mg-smectite proposed to best match the spectral properties of the most common phyllosilicate on Mars is a smectite containing a mixture of both Fe^{2+} and Mg^{2+} cations, but no Al^{3+} cations, termed "Fe/Mg-smectite" (Bishop et al., 2008a,b).

Saponite is also frequently considered the subgroup name for trioctahedral smectites; under this definition there are "saponites" with no Al^{3+} cations that resemble hectorite and there are high Al-substitution saponites that have significant substitution of Al^{3+} for Si^{4+} in the tetrahedral sheets. As it is difficult to determine the degree of Al-substitution in saponites without detailed sample characterization, this mineral name can be confusing. This confusion is often compounded because saponite is much more common on Earth than hectorite, and thus lab samples of saponite are more readily available for study. However, Mg-rich smectites do not require Al^{3+} in their structures, for example, saponite has tetrahedral substitution whereas hectorite does not.

Non-smectites. The ideal chemical formula of lizardite (Mg-serpentine) is $Mg_3Si_2O_5(OH)_4$, and that of Mg-talc is $Mg_3Si_4O_{10}(OH)_2$. For the purposes of this study, we point out that there is no aluminum in their structure. In contrast, the Mg-chlorite, clinochlore has an ideal formula of $(Mg,Fe^{2+})_5Al(Si_3Al)O_{10}(OH)_8$. A similar amount of Al^{3+} is present in micas such as the dioctahedral muscovite $KAl_2(AlSi_3O_{10})(F,OH)_2$ and trioctahedral biotite $K(Mg,Fe)_3AlSi_3O_{10}(F,OH)_2$.

3. Results

3.1 Viscosity results and ponded lava flow calculations

Table 1 presents the elemental abundances derived using SuperCam LIBS measurements on rocks from the Máaz formation, Artuby member and Séítah formation. The LIBS data are obtained from Table 2 of Wiens et al. (2022). The elemental compositions are averages over many targets within the respective units. The CIPW norm mineral sum is slightly below 100 wt% because Wiens et al. assumed a small amount of apatite based on observations of phosphorous – Ca – F/Cl/H LIBS peak associations in a few targets; however, the P, Cl, F, and H abundances are not quantified, which leads to a small mass deficit.

The CIPW norms in Table 1 provide estimated igneous mineral content in the

absence of alteration by carbonates or phyllosilicates. Wiens et al. (2022) removed observations that had clear evidence of alteration. In this paper, we will use this elemental abundance data to calculate the viscosity, and later we will discuss the low Al content of the olivine bearing unit in the Séítah unit in relation to phyllosilicate identification.

The bottom line of the table shows the calculated viscosity at 1450 K. This calculation was conducted using the Giordano empirical melt viscosity technique described earlier. The results of this calculation are plotted against the temperature in Figure 5a. We have presented the viscosity results in this manner (natural log of viscosity versus the inverse temperature) because this is the usual format of viscosity plots (e.g. Bottinga and Weill 1972, Girodano et al., 2008). We then used FLOWGO to calculate the length of the flow. We have used three different Martian viscosities and two terrestrial examples, and plotted the five lines in Figure 5b. In addition to these five examples, in Figure 5a we have also plotted the viscosity of $Di_{90}An_{10}$, which is a liquid diopside (90%) and anorthite (10%) mixture. We obtained the geochemical data for this mixture from Kirkpatrick (1974) (his Table 4) and calculated it using the Girodano et al. approach. We include it in our plot to demonstrate that liquid diopside has a higher viscosity through the relevant range of temperatures than all of our samples, except the granite. We found that $Di_{100}An_0$ has an even higher Giordano et al. viscosity, and we do not show it here.

Relative viscosity analysis. As discussed in Section 2, viscosity has a large effect on the properties of lava lakes. We showed in Figure 3b the schematic relative viscosity values for the Máaz and Séítah formations relative to the viscosity of diopside-anorthite. We are now in a position to justify this calculation. We can calculate the Giordano et al. model viscosity for diopside-anorthite ($Di_{90}An_{10}$) at 1450K as 2.58, and using the last line of Table 1, see that it lies above the viscosities at the same temperature of Séítah (0.884) and Máaz (2.46). We note that we are obliged in this comparison to estimate a temperature relevant for the lava lake model. We have chosen 1450K for comparison because it is close to the highest expected temperatures for Martian lavas (Putirka, 2016), however, we note that Figure 5a shows that $Di_{90}An_{10}$ is higher in viscosity than Séítah and Máaz for a temperature range from 800-1600K, extending the range to encompass all expected Martian lava flow initial temperatures.

Viscosity Error analysis. In order to provide some measure of the error of these viscosity derivations, we use the LIBS error estimate from Anderson et al. (2022). The average Root Mean Squared Error of Prediction (RMSEP) from their Table 5 is 1.85 wt %. Expressing this error as a percentage of a typical value of ln viscosity

of 10, we get a error band of +/- 0.185 in log units.

We also use the error estimate from Giordano et al. (2008) for their viscosity model. Giordano et al. show that the root mean square error (RMSE) of their viscosity model is 0.4 log units. We therefore use +/- 0.4 as the error band for the ln viscosity model.

Assuming that the LIBS measurement and viscosity model errors are independent, we take the square root of the sum of squares of 0.185 and 0.4 to get 0.441, and this is the total error in log viscosity that we use in Figure 5 for the error bars.

Table 1. Elemental abundances and normative mineralogies obtained using SuperCam LIBS during the Crater Floor campaign (Wiens et al., 2022). All elemental data are in wt % and the CIPW norm abundances are in %. The error on the density is discussed in Wiens et al. (2022).

Element oxide (wt %)	Máaz	Artuby	Séítah
SiO_2	54.2	49.7	44.8
TiO_2	0.6	0.9	0.2
Al_2O_3	10.5	7.4	3.9
FeO_T	20.2	25.3	22.6
MgO	2.7	3.8	21.4
CaO	5.5	7.7	3.6
Na_2O	3.3	2.7	1.3
K_2O	1.2	0.6	0.2
Quartz	5.6	0.0	0.0
Plagioclase	37.9	30.0	15.2
Orthoclase	7.1	3.6	1.2
Diopside	4.8	16.7	1.5
Hypersthene	37.9	41.5	34.7
Olivine	0.0	0.9	41.1
Ilmenite	1.1	1.7	0.4
Magnetite	1.6	2.0	1.8
An # plag	25.3	22.7	26.5
Mg #	19.3	21.1	62.8
Density (g/cc)	3.10	3.27	3.37
Error in density	±0.02	±0.03	±0.01
Viscosity at 1450° K	2.46	1.94	0.884

FLOWGO flow length results. We used the Giordano model viscosities along with PyFLOWGO to calculate the relative ability of the Martian units to flow across the Martian surface. Following Rowland et al. (2004), we used a volumetric flow rate of 4984 m^3 s^{-1}, a channel width and depth of 12.8m, Martian gravity g=3.71, a thin, cold Martian atmosphere T=206.15K, wind friction factor=0.0036, and we used a constant slope of 7 degrees in order to compare the flow distances of the units. All other parameters are identical to those in Table 1 of Rowland et al. (2004).

Figure 5b shows the runout distances in km as calculated by PyFLOWGO. We note that the distances are not the actual distances travelled on Mars, but are designed to show which units are able to flow longer distances, all things being held constant, apart from the viscosity. All our modifications to run the PyFLOWGO code are available on the Harvard Dataverse repository for the paper.

The runout distances versus eruption temperature of three Martian samples and two terrestrial samples are plotted in Figure 5b. We have chosen the terrestrial examples from Bottinga and Weill (1972) to bracket the viscosity results, the granite sample is of higher viscosity than the other four examples, and has the lowest ability to flow across the surface. The runout distance curves reflect the ability of the composition to flow, and are cut off at both ends by eruption temperature being too low and too high.

It should be noted that the dunite terrestrial sample does not display the lowest viscosity and has a reduced capacity to flow across the surface compared to the Séítah unit. In addition, the relative order of viscosities and flow distances remains granite-Máaz-Artuby-dunite-Séítah, with Séítah displaying a marked highest max run out distance in addition to being able to flow at lower temperatures than the other compositions.

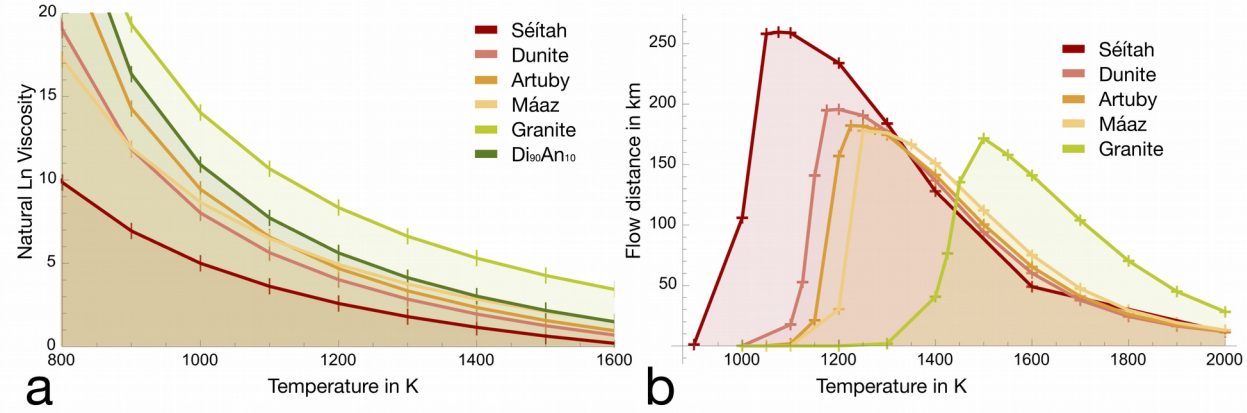

Figure 5. a.) Plot of natural log of viscosity versus temperature calculations for Máaz, Artuby, and Séítah rocks compared with terrestrial samples, including granite, $Di_{90}An_{10}$ and dunite. Viscosity error bars are +/- 0.441 and are the same for all points. b.) Flow lengths for viscosities of granite, dunite, Séítah, Artuby and Máaz on under Mars conditions (Rowland et al., 2004).

3.2. Phyllosilicate alteration

3.2.1 CRISM orbital maps

To visualize the phyllosilicates that are present in the olivine rich unit, we have produced a map of the orbital CRISM Half Resolution Long (HRL) image, HRL000040FF, over Jezero crater (Figure 6). This includes the area of Mars 2020 operations, Octavia E. Butler Landing site, Jezero Delta, and the Margin Carbonates region (Williford et al., 2018; Horgan et al., 2020; Farley et al., 2020; Stack et al., 2020). Alongside a 0.905 μm channel image, we have included three absorption band maps from the CRISM image for 2.31 μm (phyllosilicate and carbonate), 2.5 μm (carbonate) and 2.38 μm (phyllosilicate). Here we focus on the phyllosilicate signature; for more discussion of the carbonate spectral signature, see (Mandon et al., 2020; Brown et al., 2020; Zastrow and Glotch, 2021).

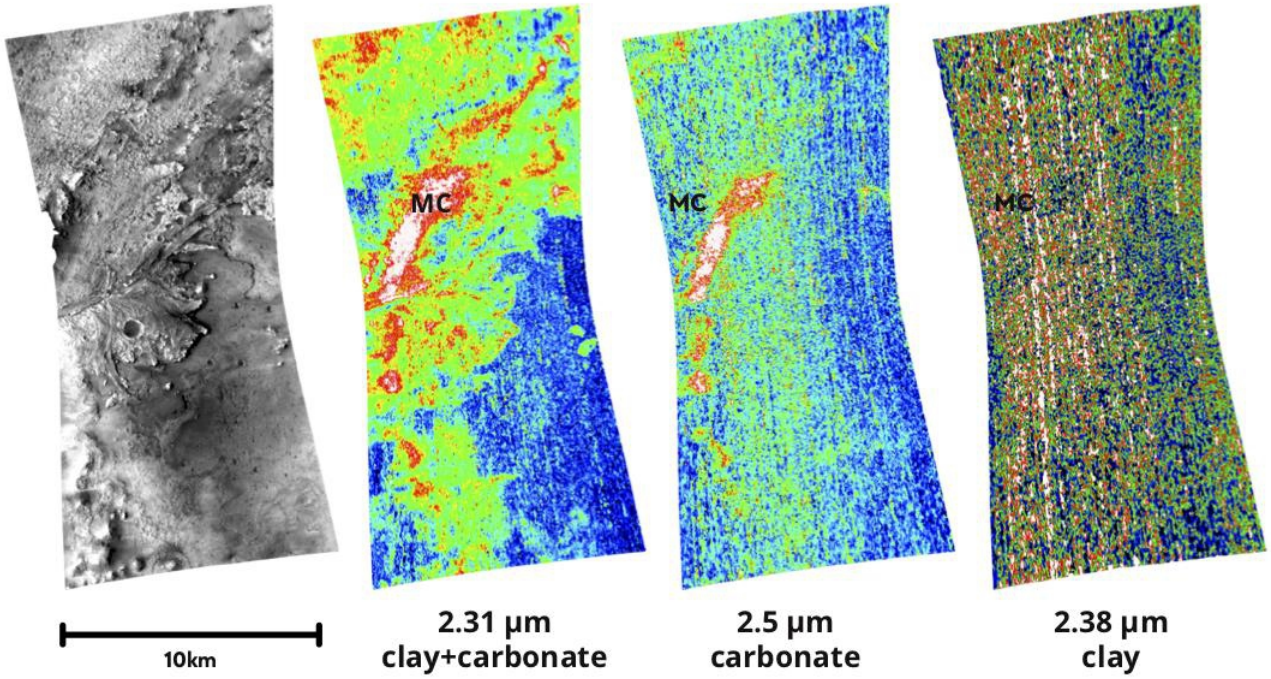

Figure 6. HRL000040FF 0.905 µm channel reflectance map, 2.31 µm, 2.5 µm, 2.38 µm band amplitude maps. The location of the Margin Carbonates is also shown as MC.

3.2.2 Correlation maps

As can be seen from Figure 6, mapping the 2.38 µm phyllosilicate band from orbit is very difficult due to it being close to the noise level. To overcome this and gain further insights into the presence of phyllosilicates in the CRISM HRL000040FF image, we have constructed a correlation map consisting of the 2.31, 2.38 and 2.5 µm bands. For each of these three band maps, we have the four parameters of the Asymmetric Gaussian band, meaning we have 12 parameters total. Figure 7 displays the correlation plots for HRL000040FF for band depth amplitude (2.38)-amplitude(2.31)-amplitude(2.5). This can be interpreted as the *x* value being the amplitude of the 2.38 µm band, the *y* value as the amplitude of the 2.31 µm band, and the coloring of the points reflects the amplitude of the 2.5 µm band.

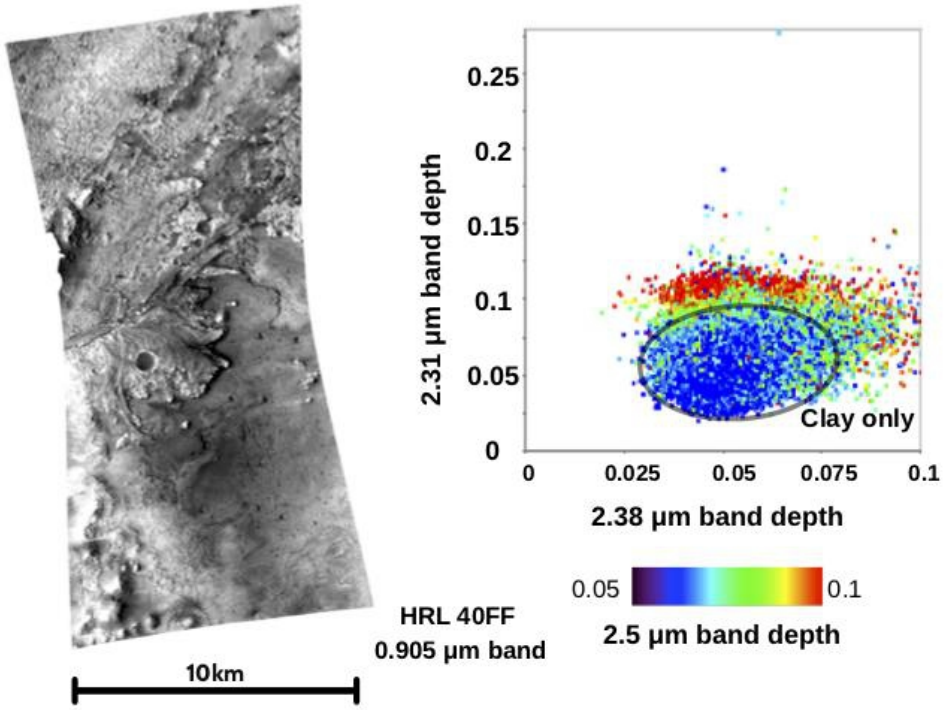

Figure 7. HRL000040FF 0.905 µm reflectance (left) and correlation plots of the 2.38 µm band depth (*x*-axis) vs. the 2.31 µm band depth (*y*-axis). Color indicates the 2.5 µm band depth, with red>green>blue.

The correlation plot shows when all three bands are present and to what degree. Figure 7 shows that the points that are high in 2.5 µm amplitude are also high in 2.31 µm band amplitude. This allows us to be very specific and make a finding: there are regions of the HRL000040FF image that display the presence of all three bands (known as the Margin Carbonates, marked on Figure 6). However, there are regions where only phyllosilicates are present, with only a weak to vanishing 2.5 µm carbonate band, indicated by blue colored points in the correlation plot on the right. This is marked "Clay only" on the Figure 7 correlation plot. Figure 6 makes clear that the highest 2.5 µm band amplitudes are correlated with the highest 2.31 µm band amplitudes. This indicates that 1) the strongest carbonates signatures are in the Margin Carbonates and 2) this is also where the strongest clay signatures are found.

3.2.3 Venn diagrammatic approach

To get a quantitative estimate of the phyllosilicate and carbonate present with the olivine in this image, we present a Venn diagram populated with data from HRL000040FF where olivine, phyllosilicate and carbonate are determined to be present. In order to construct this diagram, we used the following detection rules for the olivine, carbonate, and phyllosilicate bands, which were arrived at

iteratively to produce the least noisy CRISM maps, based on previous work (Brown et al. (2020)):

amplitude(olivine 1.0 μm band) > 0.29
amplitude(carbonate 2.5 μm band) > 0.08
amplitude(phyllosilicate 2.38 μm band) > 0.065

For simplicity and reproducibility, these rules were run on the entire georeferenced HRL000040FF CRISM image. No attempt was made (at first) to mask the image to regions of interest. We report the border pixels with no data as "edge pixels" and pixels with data as "ground pixels".

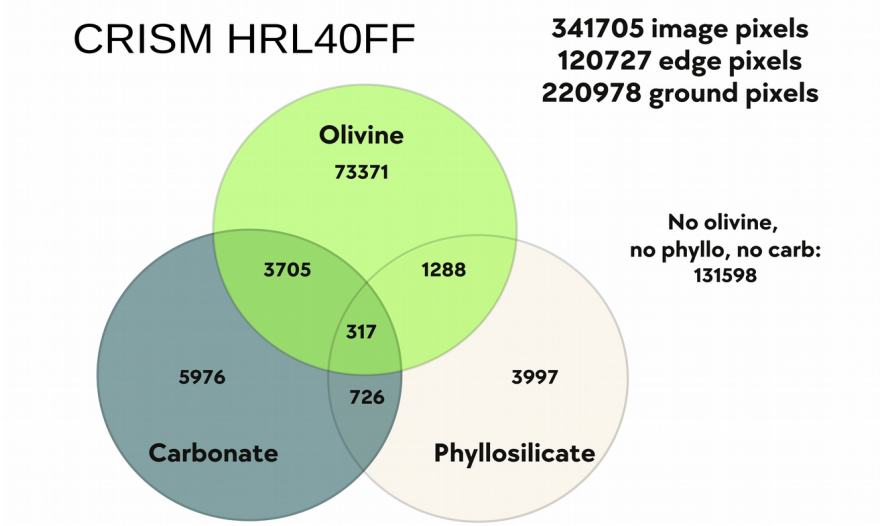

Figure 8. Venn diagram of olivine, phyllosilicate andcarbonate detections for HRL000040FF showing overlapping pixels containing olivine, phyllosilicate and carbonate. See text for details of calculation.

Figure 8 demonstrates that just more than half of the HRL000040FF image is not olivine, phyllosilicate or carbonate. Roughly one third of the ground surface pixels have olivine alone detected, which is consistent with mineral mapping presented by Parente et al. (2021). "Pure" (i.e. without the other two minerals) phyllosilicate and carbonate are present in roughly 3% and 2% of the pixels, with carbonate being more abundant than phyllosilicate, using CRISM orbital data from our study. This plot (Figure 8) also demonstrates that there are large amounts of olivine without alteration, and small but significant amounts of phyllosilicate and carbonate without significant olivine signatures in the HRL000040FF scene.

The 2% abundance of phyllosilicate containing a band at 2.38 μm from our study is consistent with the "Mg-smectite-2" unit mapped by Parente et al. (2021) with

bands near 2.30 and 2.38 μm; however, they also found additional material containing only the 2.30 μm band without the 2.38 μm band that they termed "Fe/Mg-smectite", and units of "olivine+smectite" that contain a broad band near 1 μm consistent with olivine as well as bands near 1.9 and 2.3 μm, characteristic of Fe/Mg-smectite, but no band at 2.38 μm. The Parente et al. (2021) Fe/Mg-smectite observations are consistent with past CRISM analyses of the region as well (e.g., Goudge et al., 2015) that describe the presence of Fe/Mg-smectite inside Jezero crater. Our study focused instead on the presence of the Mg-rich phyllosilicate unit that appears to contain a mixture of Fe/Mg-smectite and either talc or serpentine. The Parente et al. (2021) study also observed larger quantities of carbonate in CRISM image HRL000040FF than found in our study, possibly because their carbonate unit also contains a strong olivine-type band. See supplemental section S3 for more information and a comparison with the Parente et al. mineral map.

Séítah subset. In order to take a closer look at the Séítah region as seen from orbit, we have subset the HRL000040FF image to a smaller image of only 1750 pixels covering the Séítah region. Figure 9 displays the Venn diagram analysis for just this Séítah subset. This shows that the subset CRISM image mostly contains olivine (~95%), 2% of the pixels contain phyllosilicate and 1.5% are carbonates. Relative to the whole 40FF image, the Séítah subset contains far more pure olivine, but relatively smaller amounts of phyllosilicate and carbonate. This reflects the fact that the Séítah region carbonate and phyllosilicates are relatively difficult to detect from orbit. In the section that follows, we supplement these orbital data with in situ data from the Mars 2020 rover.

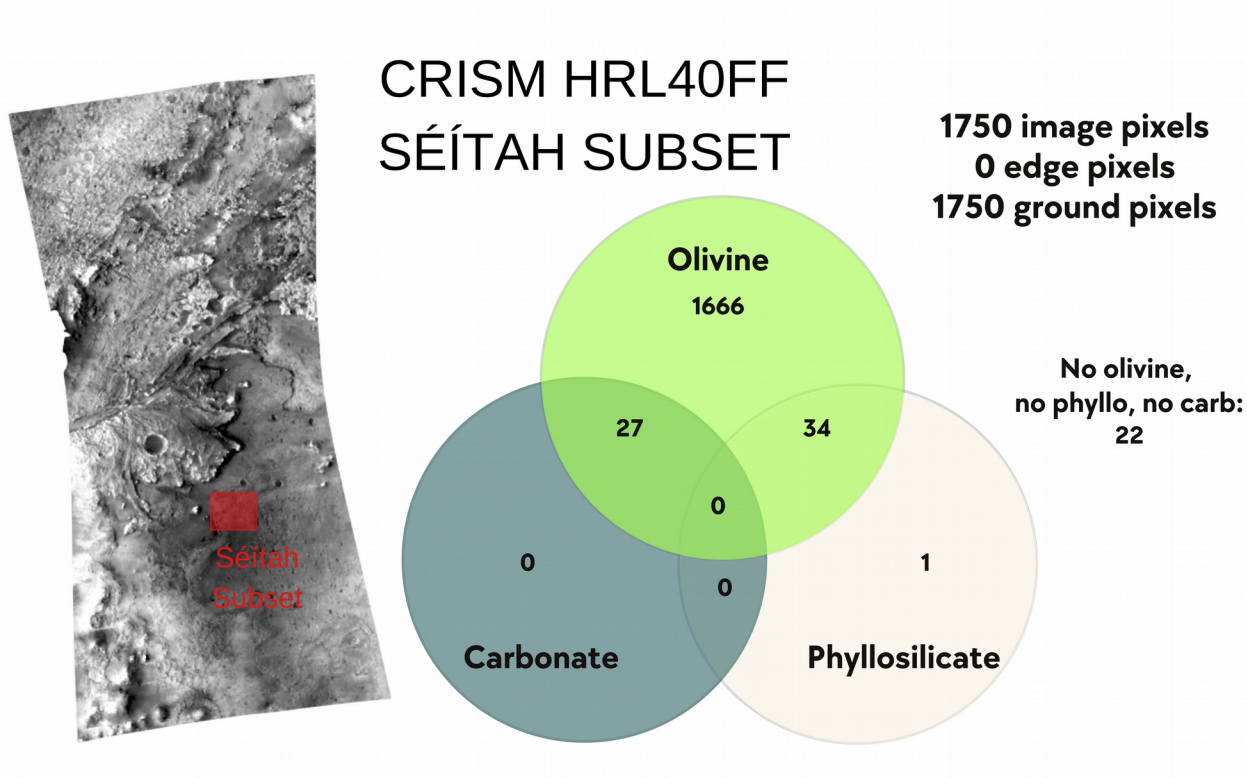

Figure 9. Venn diagram of olivine-phyllosilicate-carbonate detections for the Séítah subset of HRL000040FF, which is shown in a red box in the image at left. The diagram on right shows overlapping pixels containing olivine, phyllosilicate and carbonate.

3.3.1 VISIR In situ results

Figure 10 shows the VISIR spectra from the abraded patch named Garde taken on Sol 207 from the Séítah formation (Figure 2b). Absorption bands at 2.28, 2.33, 2.38 and possibly 2.46 µm were detected, in agreement with Mandon et al. (2023). The lack of a moderate strength 2.5 µm band suggests that this sample is not carbonate bearing; however, see the analysis by Clavé et al. (2023) in which LIBS and Raman techniques suggest small amounts of carbonate are present, and Corpolongo et al. (2023) in which SHERLOC Raman analyses of the abrasion patch indicate carbonate. The presence of bands at 1.9, 2.28, 2.31, 2.38 and at 2.46 µm in the VISIR indicates that the Garde sample is phyllosilicate bearing. In addition, although weak, there is a band present in the spectrum at 2.1 µm, and though this is a little offset (2.09 µm), this band is also present in talc. Finally, the 2.46 µm band in serpentine is far weaker than in talc. Figure 10 also shows the example of a spectrum from Dourbes_Tailings_255 which shows the most convincing example we have found of bands at 1.94, 2.28, 2.31, 2.38 and at 2.46 µm, thereby constituting the strongest evidence so far in the Séítah formation for

the presence of talc, in agreement with Mandon et al. (2023).

Also shown in Figure 10 are talc, serpentine (lizardite), hectorite, saponite, Fe/Mg smectite and stevensite spectra from Figure 4 for direct comparison with the band positions of the VISIR data.

Table 2 is a summary of the band positions that are present in each of the minerals and targets that are present in Figure 10. Red text indicates a band is weak or missing in this location. An asterisk indicates the presence of a shoulder band.

Table 2. Assessment of SWIR band positions for elements in Figure 10. All values are in μm. Asterisk indicates shoulder bands, red text indicates missing or weak band.

Target	1.9-1.97	2.0-2.1	2.1-2.16	2.25-2.29	2.29-2.35	2.35-2.40	2.40-2.5
Garde 207	1.94	2.08	2.14	2.28*	2.32	2.39	2.46
Dourbes Tailings 255	1.94	2.08	2.14	2.28*	2.32	2.39	2.46
Talc TL2702	1.91	2.08	2.14	2.28*	2.31	2.39	2.46
Lizardite NMNHR4867	1.97	2.08	2.14	2.29*	2.32	2.39	2.46
Fe/Mg Smectite	1.91	2.08	2.14	2.28	2.32*	2.39	2.46
Hectorite	1.91	2.08	2.14	2.29*	2.31	2.39	2.45
Saponite	1.91	2.08	2.14	2.29*	2.31	2.39	2.46
Stevensite	1.91	2.07	2.12	2.29*	2.31	2.39	2.47

Based on Table 2, the lack of a 2.46 μm band is somewhat problematic for lizardite and Fe/Mg smectite, however the 2.46 μm band in Dourbes is so weak that it can hardly be disqualifying. At this stage, we see advantages to keeping all 6 candidate minerals in the mix, in the anticipation of spectra with stronger absorption bands later in the mission.

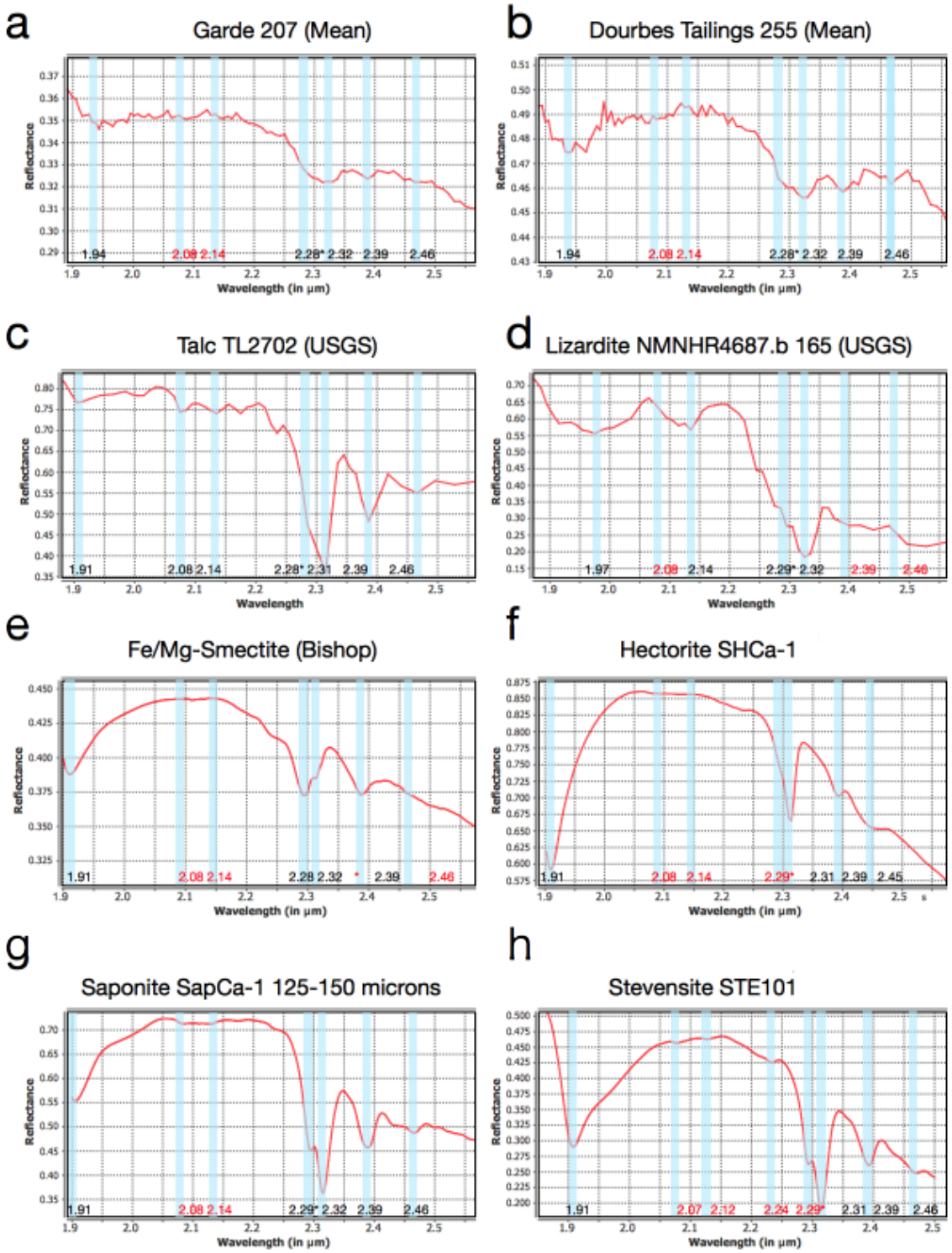

789 Figure 10. VISIR spectra of a. Garde_207 and b. Dourbes tailings from Sol 255 and plots of the USGS
790 spectroscopy library spectrum of talc, lizardite, Fe/Mg smectite, hectorite, saponite and stevensite from
791 Figure 4. Red text indicates a weak or missing band, and an asterisk is a shoulder band.
792
793

3.3.2 VISIR, RMI and Mastcam-Z tailings observations

Figure 11 shows the MastCam-Z image for the Dourbes target (abraded rock, Figure 2c), showing the tailings that were captured by the VISIR instrument. It should be noted that the tailings are relatively bright, especially compared with the surrounding bedrock, which is again consistent with the presence of talc or hectorite, which both have high reflectance (>0.9 in the visible region). It should be noted that a decrease of grain size will also increase the albedo, so we do not consider the brightness change to be definitive evidence for talc/hectorite over the other phyllosilicates.

Also shown in Figure 11 are the spectra from the VISIR observations of targets Dourbes, Salette and Brac, which are shown with the spectra of the original rock surface and the tailings after abrasion. The Dourbes exampleshows a relative overall increase in albedo, and the appearance of a band at 2.46 μm which is not present (or only weak) in the original rock. This is strongly suggestive that the Dourbes tailings have made the presence of the phyllosilicate more obvious in the spectra, and because the 2.46 μm band is not present in lizardite (Figure 10), this also suggests the tailings contain the mineral talc.

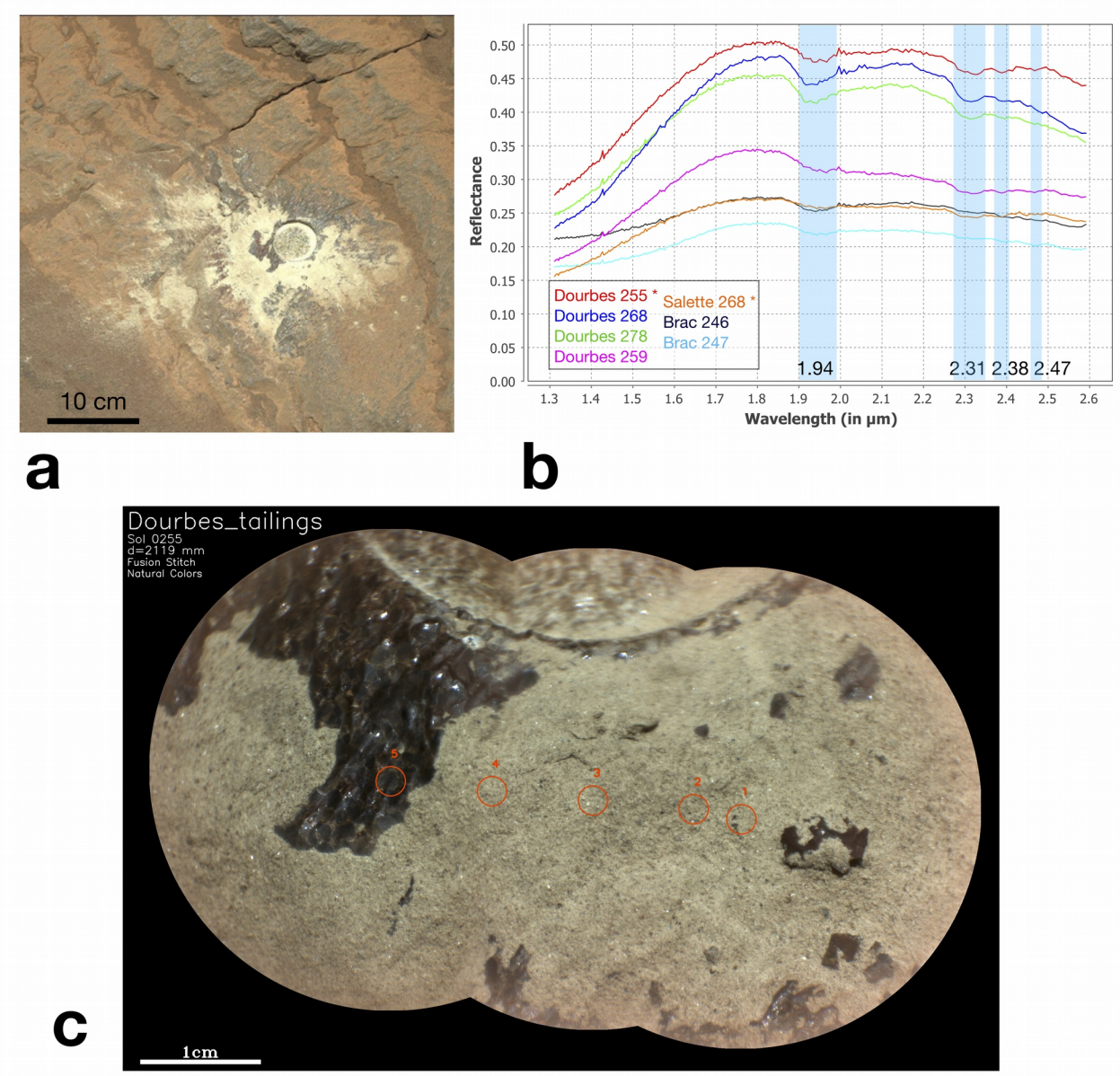

Figure 11. a.) Mastcam-Z of Target Dourbes with tailings on Sol 255 after abrasion in the Brac workspace. Note the brightness of tailings compared to the original rock surface. b.) Spectra of the tailings compared to the original rock surface. Spectra of tailings are marked with an asterisk (*). Vertical cyan bars indicate key spectral bands. Note the presence of the 2.46 µm band in the Dourbes tailings spectra c.) SuperCam RMI image of target Dourbes tailings after abrasion. The numbered red circles indicate the locations at which the data was taken for the Dourbes 255 tailing target and their fields of view (65% of total signal encircled). The blue spectrum in (b) corresponds to the average of the red circles in (c).

3.3.3 SuperCam LIBS ternary plot

Figure 12 shows a Si+Al,Fe+Mg,Ca+Na+K ternary diagram displaying the SuperCam LIBS elemental composition results up to Sol 466 of the mission in black/grey and 10 orange points measured on the target Ubraye_255 which is a rock located near the Dourbes abrasion patch showing cumulate texture (Liu et al., 2022) in the Brac workspace (Figure 2c). The elemental composition lies very close to the olivine calibration target and also overlaps with the region of talc and serpentine. Given how close these points are and the errors inherent in the planetary LIBS observations (Anderson et al., 2022) it can become challenging to tell these mineral compositions apart by just looking at the major elements. We provide in the supplementary section S4 a discussion of errors and discrimination of points in the ternary plot.

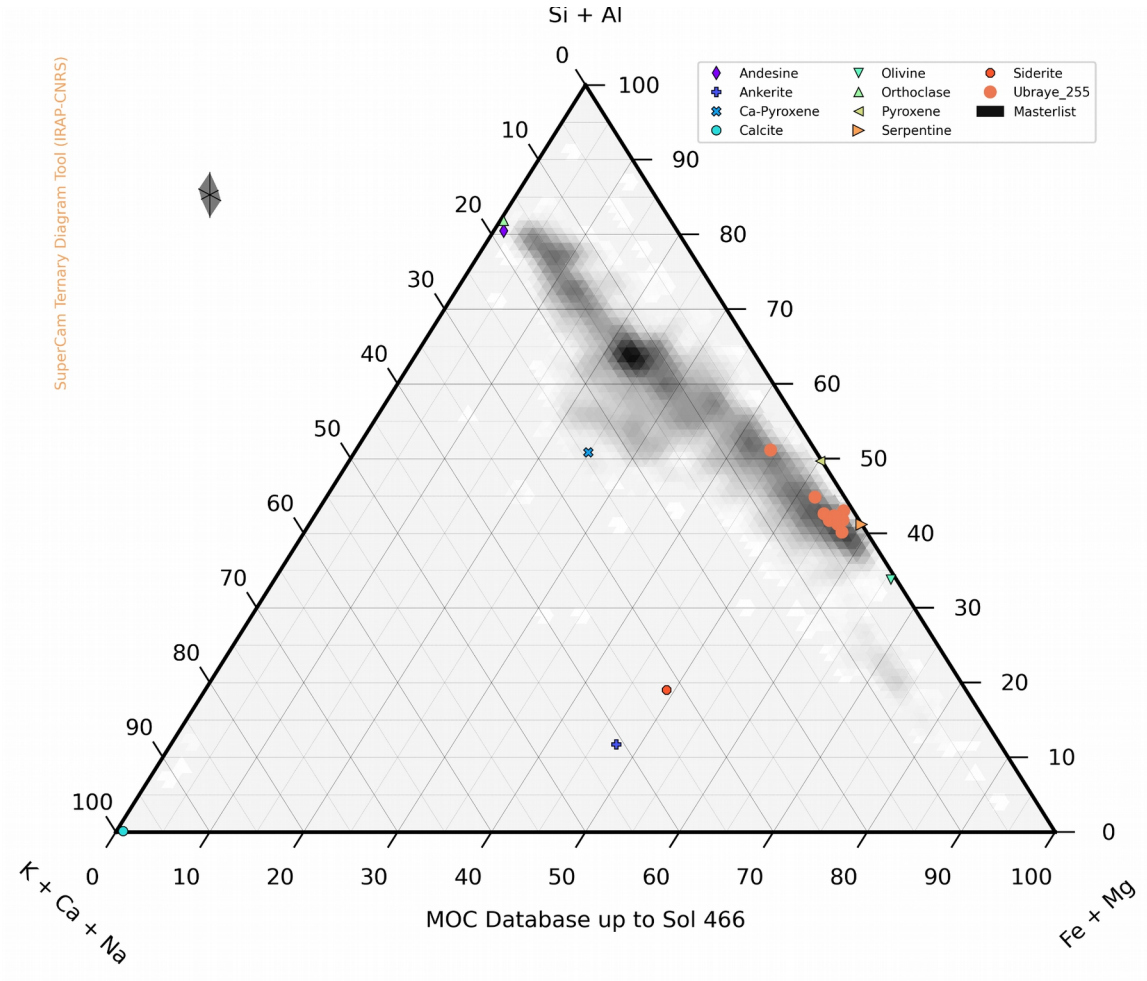

Figure 12. LIBS and geochemistry ternary molar plot indicating Ubraye_255 (orange circles without outline) cumulate target showing overlapping olivine (green inverted triangle) and serpentine (right-pointing orange triangle) standards on board the rover. The gray polygon at top left above the main figure indicates the precision error bars of the plot. MOC is “Major-element Oxide Compositions”.

Low Aluminium. Table 3 gives an example composition from targets Cine and Ubraye showing the very low (<4 wt %) Al present in these samples. Wiens et al. (2022) Figure 2f shows a cumulate texture in the target Cine. Anderson et al. (2022) Table 5 gives the mean accuracy of the Al_2O_3 estimate at +/- 1.8wt %. For these LIBS targets (Cine/Garde, Ubraye/Dourbes which are all in the Séítah region) we can thus eliminate the possibility of Al-bearing phyllosilicates.

Table 3. SuperCam LIBS Elemental abundances from targets Cine_206 (cumulate rock next to Garde in Bastide workspace) and Ubraye_255 (cumulate rock near Dourbes in Brac workspace). Cine_206 point 3 and 5 and Ubraye_255 points 1-4 and 6-10 show a very low amount of Al to within error (<4%) in the cumulate textured rocks. Green boxes highlight the high values of FeO_T and MgO and red boxes highlight the low values of Al_2O_3. S.D. is the standard deviation for that elemental data. Specifically, it is the S.D. of the 25 single shot spectra averaged in each case. All elemental abundance data are in wt %.

Target	#	SiO_2	SiO_2 S.D.	TiO_2	Std Dev	Al_2O_3	Al_2O_3 S.D.	FeO_T	FeO_T S.D.	MgO	MgO S.D.	CaO	CaO S.D.	Na_2O	Na_2O S.D.	K_2O	K_2O S.D.	Total
Cine	1	44.99	1.19	0.43	0.02	3.27	0.53	13.37	1.52	11.54	1.16	15.84	0.68	0.39	0.13	0	0.17	89.83
Cine	2	51.05	1.9	0.04	0	2.94	0.97	25.74	2.06	13.4	1.96	4	0.5	1.19	0.38	0	0.15	98.36
Cine	3	45.13	2.03	0.01	0.02	0.87	0.95	34.59	2.13	28.93	1.27	1.81	1.09	0.37	0.33	0	0.05	111.71
Cine	4	43.39	1.15	0.45	0.03	3.91	1.34	10.43	2.41	11.13	0.92	13.72	0.79	0.49	0.17	0	0.19	83.52
Cine	5	45.34	2.14	0.01	0.01	2.89	1.08	36.37	3.56	28.35	2.22	1.28	0.48	0.51	0.11	0	0.03	114.75

Target	#	SiO_2	SiO_2 S.D.	TiO_2	Std Dev	Al_2O_3	Al_2O_3 S.D.	FeO_T	FeO_T S.D.	MgO	MgO S.D.	CaO	CaO S.D.	Na_2O	Na_2O S.D.	K_2O	K_2O S.D.	Total
Ubraye_255	1	48.72	2.07	0.01	0	2.02	0.88	24.5	2.92	31.5	0.85	1.43	0.54	1.22	0.21	0	0.23	109.4
Ubraye_255	2	44.76	2.2	0.01	0	2.25	0.88	25.94	2.24	27.91	2.7	1.25	0.37	0.34	0.09	0	0	102.46
Ubraye_255	3	51.41	2.57	0.02	0.01	1.57	1.06	23.63	3.05	32.07	0.85	0.8	0.4	1.37	0.17	0.49	0.41	111.36
Ubraye_255	4	45.97	1.52	0.01	0	1.79	0.75	26.35	2.87	28.87	2.03	1.32	0.36	0.3	0.1	0	0.03	104.61
Ubraye_255	5	49.34	2.74	0.04	0	3.92	1.14	28.53	3.78	15.25	2.62	1.65	0.44	1.32	0.14	0.52	0.38	100.57
Ubraye_255	6	46.36	1.4	0.01	0	1.78	1.11	21.35	1.86	30.32	1.16	0.56	0.21	0.29	0.05	0	0.15	100.67
Ubraye_255	7	43.03	7.28	0.03	0.01	2.59	1.32	27.74	3.44	26.59	0.89	1.52	0.42	0.65	0.13	0	0.12	102.15
Ubraye_255	8	47.04	1.74	0.01	0	1.67	0.72	23.18	2.38	29.89	1.04	1.41	0.34	0.65	0.17	0	0.07	103.85
Ubraye_255	9	45.92	2.24	0.49	0.11	3.47	0.79	25.17	2.79	24.79	0.66	1.53	0.3	0.97	0.18	0	0.04	102.34
Ubraye_255	10	45.84	2.18	0.01	0.01	0.54	0.67	27.48	2.68	28.97	2.2	1.46	0.21	0.76	0.15	0	0.03	105.06

4. Discussion

With the insights now gained from bringing together orbital and in situ observations, we now discuss two aspects of the geological history of the olivine rich lithology.

4.1 Emplacement of olivine rich lithology and exposure today

Figure 5 shows that the Séítah formation composition leads to a low viscosity lava that is able to flow over relatively long distances. Although terrestrial komatiite lavas have an even lower viscosity, the Séítah formation and similar olivine rich units throughout Mars may also lead to similar coverage characteristics mirroring that of komatiites on Earth. The low viscosity is due to the low Al and Si and high Mg and Fe of the formation. The low Al is also directly linked to the olivine and alteration phyllosilicates we have analysed in this paper.

Given the low viscosity for the lithology calculated in this paper, the results of RIMFAX (the Ground Penetraing Radar instrument on the Mars 2020 rover) showing the relatively thick volcanic or sedimentary layers (Hamran et al. 2022), and the lack of low shields in the local Jezero region from orbital mapping, we consider it likely the olivine at the Séítah formation was emplaced as a ponded lava flow. Future observations at the Margin Carbonates and outside Jezero will test what other formation mechanisms are involved in other parts of the lithology.

Under the ponded lava flow hypothesis, the olivine rich lithology was likely variable in thickness, and in catchment regions of deep relief, such as Jezero crater, the flow would likely have formed a lava lake several tens of meters thick.

Effect of viscosity. Worster et al. (1993) presented a model of heat flow in a lava lake cooled from above and insulated (or cooled) from below, and utilizing the balancing of the heat equation with crystallization of the melt, they could estimate the total crystallization amount. Their results are shown with their model in Figure 3. Figure 3b also shows that for inferred viscosities typical of the Séítah elemental composition, using the two base cooling scenarios as error bounds, the formation of crystals in the mushy layer and accumulating on the floor could have filled up to ~40%+/-10% of the volume of the lake. The Worster et al. (1993) model was based on experiments using liquid diopside-anorthite, and was intended to be extendable to lower viscosity units such as olivine cumulate, so it is relevant to our Martian scenario.

Very fluid lava flow episodes have been described in the case of rather recent volcanic events at Central Elysium Planitia (Vaucher et al., 2009) and the Tharsis region (Mangold et al., 2010). The combined mineralogical and petrophysical information gained at Jezero with this current study of Séítah unit is supportive of the hypothesis that low viscosity lava flows did occur, possibly at large scale, early in the Martian history; as such, it may place valuable constraints on the composition of the Martian interior during the early to intermediate stage of chemical differentiation (Grott et al., 2013).

Depth of ponded lava lake. We suggest that the rocks of the ponded lava lake have been eroded back to reveal the cumulate portion of the lava lake and then covered by crater fill consisting of igneous material from later eruptions such as the Máaz formation (Udry et al., 2023) and Artuby member of the Máaz unit (Alwmark et al., 2023) which has itself then been eroded back in locations to reveal the olivine rich lithology beneath it. Ground-penetrating radar imaging performed by RIMFAX in the vicinity of Séítah reveal sub-horizontal high-amplitude reflectors down to 15 m burial depth including lenticular reflector geometries interpreted to most likely represent cross-sections of igneous flow lobes (Hamran et al., 2022) The base of the Séítah unit currently remains unclear, but is at least ~15 m below the surface at the deepest locations observed so far by RIMFAX.

Assuming for the sake of the argument that the Séítah formation was ~10 m deep and it was formed as a lava lake, this suggests (using Figure 3b) that approximately the lower ~4+/-1m consists of the cumulate olivine observed at Bastide workspace (Figure 2b).

4.1.1 Spatial distribution of lithology as ponded lava flow

Wilson and Head (1994) suggested that lava flows on Mars will extend further than lava of the same composition on Earth. As mentioned in Section 2, Rowland et al. (2004) showed that in fact Martian lavas will be about 60% as long as terrestrial flows, due to the lower gravity and the lower pressure of the current Martian atmosphere. A higher pressure Noachian atmosphere would decrease the runout. Assuming that the olivine rich unit mapped from orbit is associated with the Séítah formation olivine, the flow would have covered a significant portion of the planet (Figure 13). Kremer et al. (2019) mapped the unit to extend over both sides of the Nili Fossae, and showed the unit to be predominantly exposed on the eastern side of the Nili Fossae, and truncated by Syrtis Major to the south, and later cratering activity, most notably by Hargraves Crater in the middle of the two predominant Fossae. Considering only the region of the Isidis Planitia basin

complex currently covered by the olivine rich lithology (e.g. Kremer et al. (2019) and Brown et al. (2020)), and excluding the olivine on the Libya Montes region on the southern edge of the basin (Tornabene et al., 2008), this area extends roughly 500 km north to south and 350 km east to west and is approximately the size of Florida (in 2022) in the United States (~170,000 km^2).

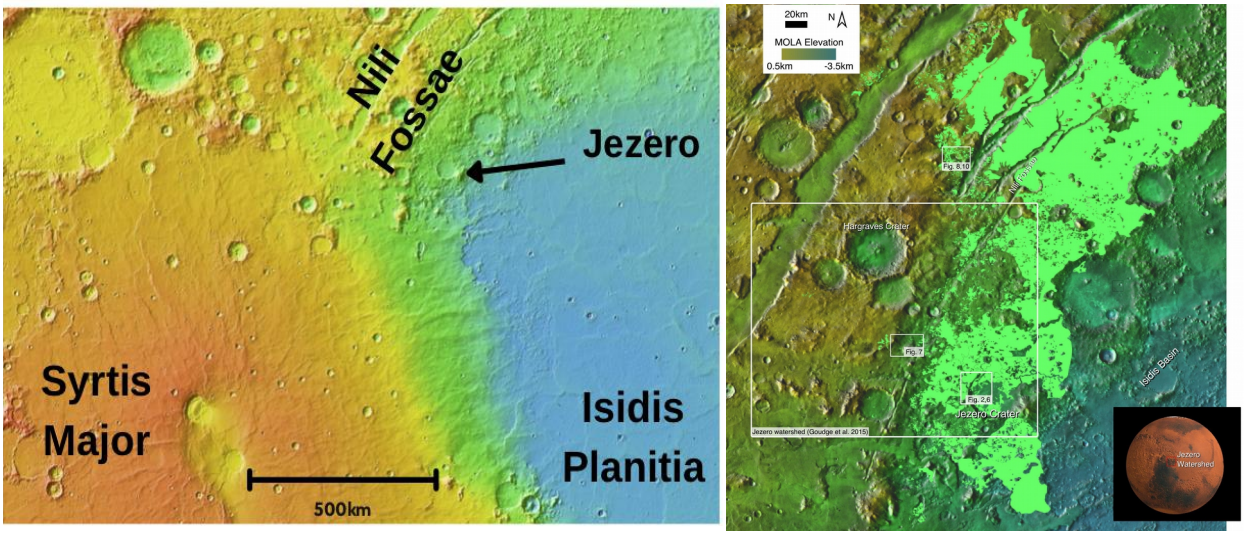

Figure 13. a.) MOLA image showing the relationship of western edge of the Isidis Basin complex, giving the relative positions of Syrtis Major, Nili Fossae and Jezero Crater. b.) Figure 1 of Brown et al. (2020) showing the extent of the olivine rich lithology as mapped by Kremer et al. (2019) in a region about the size of Florida. Note obscuration by later crater ejecta blankets, especially Hargraves Crater.

The potnetial contact between the Syrtis Major lavas and the olivine rich lithology is striking and leads one to conjecture whether the Fossae is present beneath the Syrtis Major construct; although this has not been previously addressed, we will now postulate about how this geophysical relation might have occurred. Rampey and Harvey (2012) identified the wide depressed footprint of Syrtis Major and suggested that:

> "early eruptions at Syrtis Major might have consisted of voluminous low-viscosity, possibly komatiitic magmas, whose powers of thermal erosion … may have been responsible for the wide, depressed footprint of Syrtis Major."

And at the end of the same paragraph:

> "... the youngest and most visible surface rocks of which would be basaltic komatiites, but whose earlier, more voluminous rocks would have been ultramafic. In the absence of tectonic effects these deep-seated rocks would have restricted exposure."

We would contend that the missing earlier, more voluminous ultramafic rocks, are, in fact, the olivine-rich lithology we have been studying.

Somewhat more speculatively, we might make some passing comments which may be useful to test in future investigations. The suggestions are four-fold and currently have no basis in observation, but are consistent with observations so far and may be tested in future observations, for example when the *Perseverance* rover can inspect the Nili Fossae in situ.

1) The fissures that were the source of the olivine lava flow were possibly linked to, or in fact used, the Nili Fossae fractures on the northwest of Isidis Planitia, and opened after the Isidis impact (Wichman and Schultz, 1989). The analogy might be made to the hypothesized relationship between Cerberus Rupes and Cerberus flood lavas (Plescia, 1990) in Central Elysium Planitia.
2) At Cerberus, it is possible that the flood lava evolved to a plains style lava. This may also have happened in the Isidis basin, where Syrtis Major may have been created after fissure lavas became more viscous, and the Syrtis shield may now cover fissures from an earlier phase of flood volcanism that produced the olivine-phyllosilicate-carbonate lithology. Figure 13 shows a Mars Orbiter Laser Altimeter (MOLA) altimetry map of the region highlighting the spatial relationships between the Isidis, Syrtis, Nili Fossae and Jezero crater. Rampey and Harvey (2012) suggested that Syrtis Major evolved from ultramafic to mafic over time and that super-hot komatiite lava may have eroded basement rocks. However, it is possible that evidence of this olivine may yet be found buried at depth by Syrtis Major lavas. Channelized lava flows travel much further than non-channelized flows (Pinkerton and Wilson, 1994), and the last Syrtis Major lavas may have traveled more easily in the Nili Fossae graben and subchannels.
3) At Cerberus, the lavas are much younger than the olivine lava flow, post-date water-related fluid channels, and are often guided by those channels. Volcanic activity commenced at Syrtis between 3.6-3.9 Ga (Robbins et al., 2011) around the same time as the oldest deposits on Tharsis were emplaced at 3.67 Ga (Isherwood et al., 2013). The age of the olivine (3.82 +/- 0.07Ga, Mandon et al. (2020)) would imply that no surface water channels were available to confine the flow, but might instead be governed by the widespread emplacement of the Noachian basement rocks.
4) During emplacement of this ponded lava flow, it might be possible that Séítah sank into and eroded the regolith it was laid down upon (Huppert et al., 1984). Evidence for all four of these suggestions might be found in exposures sounded by RIMFAX during the Mars 2020 mission in the Outside Jezero part of the mission.

4.1.2 Properties of cumulate layer and terrestrial analog

Huppert and Sparks (1981) discuss the manner in which an olivine bearing ultramafic cumulate layer might form in a magma body beneath a less dense plagioclase bearing basaltic layer. This model is a reasonable candidate for the formation of the Séítah formation and the Artuby member of the Máaz formation (see also Crumpler et al., 2023). It may even be possible that the lava which formed Séítah was contaminated during eruption and emplacement (Huppert and Sparks, 1985), and given its low viscosity and high temperature, this may have differentiated the upper Issole member as a contaminated version of the lava producing the lower cumulate Bastide member (Crumpler et al., 2023).

Figure 14 compares the Martian olivine cumulate target Cine_206 and the terrestrial olivine cumulate target AJB0503100 from the Dresser Formation in the Pilbara Craton of Western Australia. Both show equant (1 to 1.5 mm diameter) grains that are interlocking. Both were likely formed as the basal part of a lava flow or ponded lake when the olivine crystals fell out of suspension and collected at the basal cumulate layer. The terrestrial example on the right in Figure 14 was sampled from the talc-carbonate altered unit at the bottom of the Mt Ada Basalt in the Dresser Formation of the North Pole Dome in the Pilbara region of Western Australia. The sample is part of a komatiite sequence and specifically the B2 adcumulate layer (Arndt et al., 2004). We have shown in this paper that the target Cine shares many spectral, mineralogical and morphological characteristics of the terrestrial target. Although a Martian lava flow is likely to have formed from a cooler mantle source than the terrestrial komatiite (Putirka, 2016), we contend that it is the viscosity we have derived here that governs emplacement properties of the lava flow. Direct comparison of the viscosity of the two units is challenging due to the high Mg nature and alteration of the terrestrial sample (MgO 18.9 wt.%, FeO_T 7.6 wt.% from microprobe, presented in Brown (2006b)) versus the higher Fe content of Target Cine (SiO_2 45.24 wt %, MgO 28.64 wt.% and FeO_T 35.48 wt.%, which is the average of Cine points 3 and 5 from Table 3). It should be noted that the composition of both these rocks does not represent the bulk composition of the magma because they are cumulates of material that were sourced from elsewhere, most likely within the upper zone of the ponded lava flow.

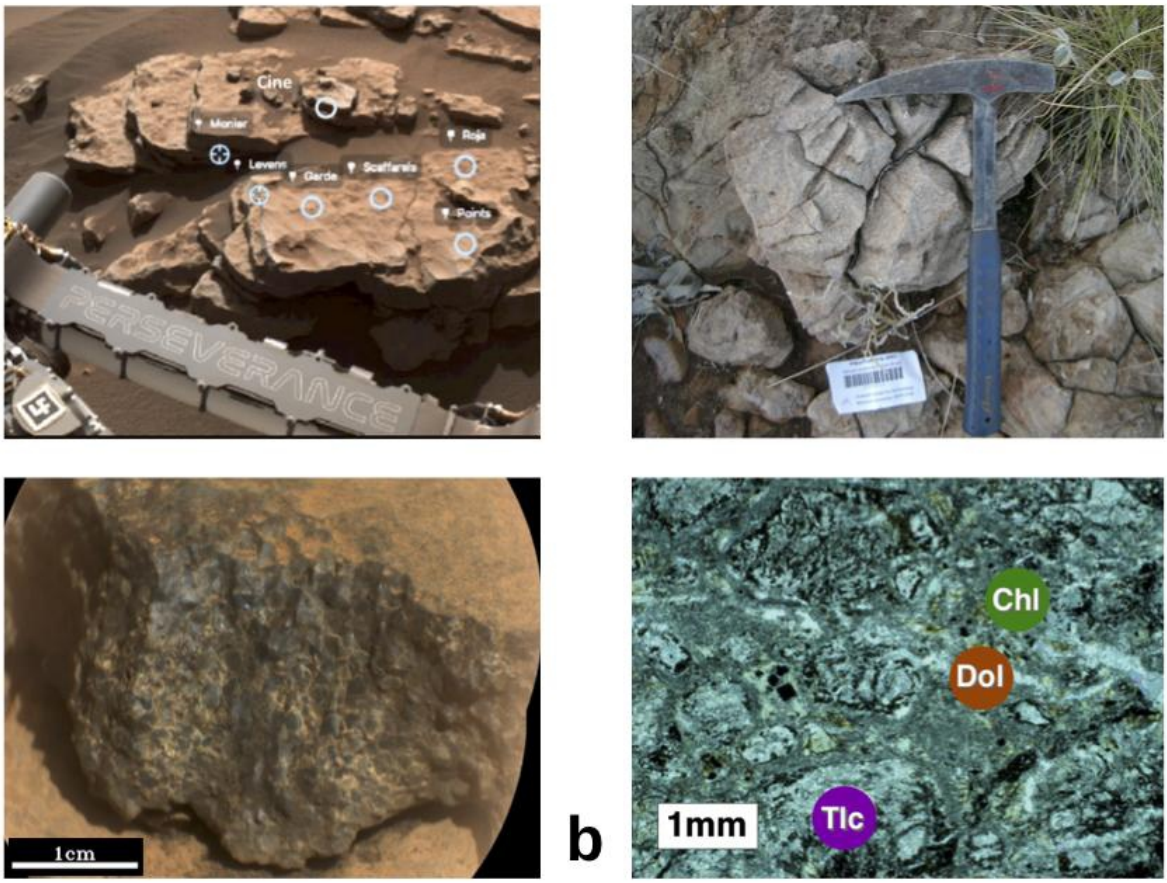

Figure 14. a.) (bottom) SuperCam RMI of target Cine showing olivine cumulate texture at mm scale. (top) Bastide workspace, location of Cine relative to Garde, rover nameplate is ~8 cm wide. b.) (bottom) Thin section of talc-carbonate sample AJB0503100 from Brown (2005; 2006b) with mm size talc (Tlc) replacing olivine, dolomite (Dol) and chlorite (Chl) identified using electron microprobe. (top) Context image for target AJB0503100 with hammer for scale.

4.2 Limited Post emplacement phyllosilicate-carbonate alteration

The fact that ~3.82 Ga olivine is still well preserved on Mars and relatively unaltered speaks volumes to the amount of alteration and volatiles present on Mars. In terrestrial greenstone Archean terranes, olivine is usually only present as a polymorph of its former self, often replaced by phyllosilicates such as serpentine or talc (Figure 14b).

Wilson and Head (1994) suggest that lavas on Mars have fewer volatiles than lavas on Earth. Despite this, the low amount of alteration present means it is still possible that the alteration fluids were juvenile water and CO_2, sourced from the fissure, as suggested and discussed by Brown et al. (2020).

The limited extent of post emplacement phyllosilicate and carbonate alteration is

evident from the Venn diagrams we have presented in Figures 8 and 9, and is also the subject of two other studies, including phyllosilicate (Mandon et al., 2023) and carbonate (Clavé et al., 2023). Mandon et al. (2022) show that in olivine-carbonate-serpentine mixtures, the bands of serpentine are deep for percentages of < 5 wt.% of serpentine (with grain size dependencies). This also has implications for the alteration history, as the rocks in the Séítah formation might not have extensively interacted with fluid compared to some other parts of the regional olivine unit, which appear more altered from orbit.

4.3 Other emplacement models

There are a number of aspects of the regional morphology and properties of the olivine-rich lithology that remain poorly understood, including draping morphology and laterally continuous layering and lack of clear lava flow features. These have been used to argue in favor of an explosive volcanic origin for the lithology (Rogers et al., 2018; Kremer et al., 2019; Mandon et al., 2020; Ruff et al., 2022). Wilson and Head (1994) modeled clasts with diameters between 100 μm and 10 mm and maximum travel ranges of pyroclasts in current day (6 mbar) Martian atmosphere for eruption cloud heights from 50-300 km. Their Figure 21 demonstrated that the maximum range drops sharply as grain size increases. They also presented a modeled maximum pyroclastic flow run out length as a function of eruption velocity for three different surface friction coefficients. Their Figure 23 shows that the 1.5 mm olivine grain size would only travel about 20 km away from the vent through pyroclastic fall, and thus far, the Mars 2020 team is yet to discover pyroclastic signatures (e.g. fiamme) in the imagery of abrasion patches obtained by the rover.

4.4 Future prospects and Mars Sample Return

At the time of writing this paper and other accompanying papers in the Jezero Crater Floor collection, the ongoing progress of the *Perseverance* rover has brought it to the Jezero Delta campaign of its mission. Within the delta, the delta curvilinear unit (*DCu*) and some parts of the delta have been documented to contain carbonates, from orbital studies (Goudge et al., 2015, 2018), and are now being characterized by surface observations (Mangold et al., 2021). We anticipate unexpected findings in the rocks and cobbles of the delta, which will provide us views of the outside watershed at irregular intervals. Figure 15 gives the timeline of events in Martian geological history that are critical to understanding its evolution and reliance upon regional and global events. We point out that this timeline shows an approximate correlation between the Jezero Delta and the

recently hypothesized second generation ocean, called Deuteronilus, aged approximately at 3.65Ga, and discussed in Citron et al. (2018) which they hypothesized filled Isidis with water. The existence and timing of these oceans is a source of ongoing debate (Sholes et al., 2021; Sholes and Rivera-Hernández, 2022) and during the Delta campaign we may hope to deepen our understanding of the source of the water that once filled Jezero.

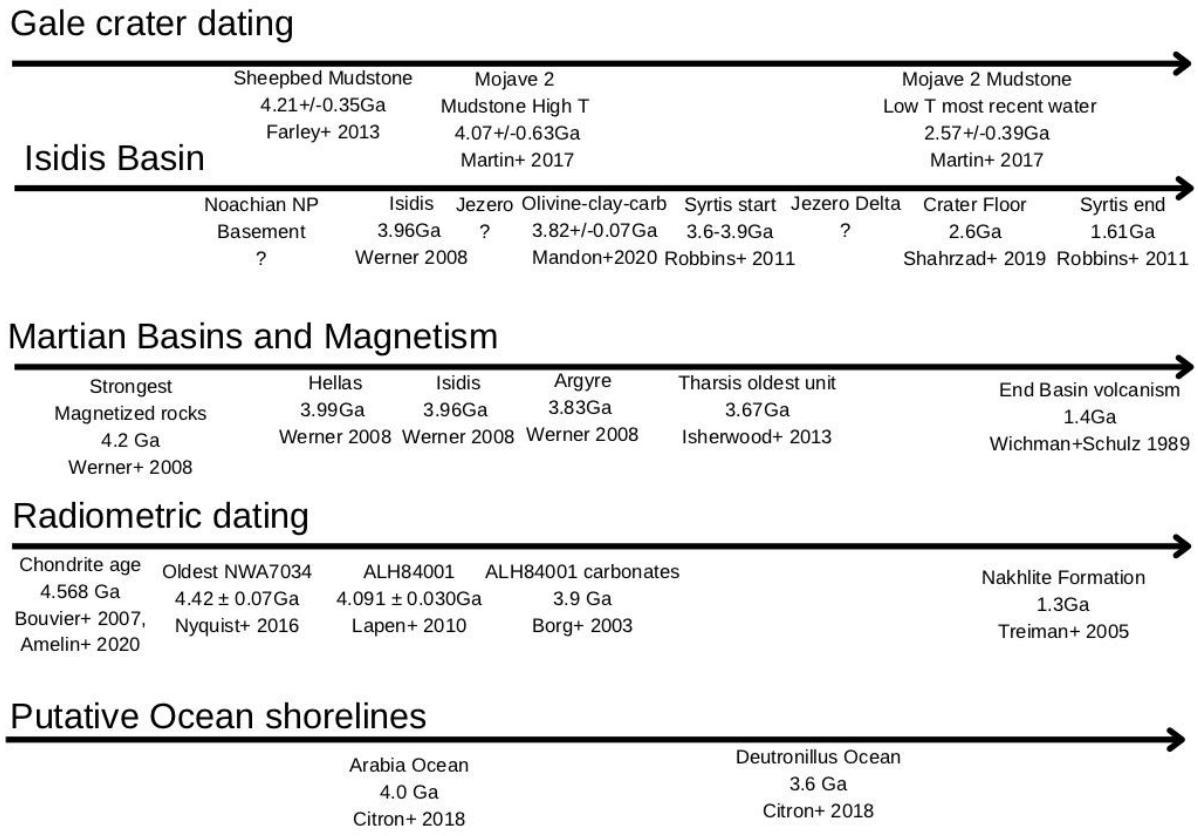

Figure 15. Timeline of events relevant to the emplacement and retention of the olivine-rich lithology. Dates are from various sources (Amelin et al., 2002; Borg et al., 1999; Citron et al., 2018; Farley et al., 2013; Isherwood et al., 2013; Lapen et al., 2010; Mandon et al., 2020; Martin et al., 2017; Nyquist et al., 2016; Robbins et al., 2011; Shahrzad et al., 2019; Treiman, 2005; Werner, 2008; Wichman and Schultz, 1989). NP = Nili Planum

After the Delta campaign, the rover will pass either nearby or through the Margin Carbonates, which are the greatest concentration of carbonates at Jezero (Figure 6).

Throughout its mission *Perseverance* is collecting samples for later return to Earth as part of the Mars Sample Return Mission. The samples collected in the Crater Floor campaign are discussed in Simon et al. (2023). Upon return to Earth, we anticipate these activities to test the postulates and expand the findings of this paper:

* Use of radiometric age dating on the grains and mesostasis,
* Determination of phyllosilicate and carbonate type using Microprobe and X-ray Diffraction,
* Determination of phyllosilicate and carbonate relative timing using X-ray tomography,
* Source of carbonate using stable isotopes,
* Age dating of delta topsets and bottom sets samples to constrain the age of the Jezero Delta.

5. Conclusions

The *Perseverance* mission completed the Crater Floor science campaign in April 2022, and thus the observations and interpretations we have reported here are limited to the olivine-rich lithology as it appears at the Séítah formation. We can infer characteristics of the unit beyond Jezero based on orbital observations (Goudge et al., 2015; Horgan et al., 2020; Mandon et al., 2020; Brown et al., 2020). For example, one observation of the orbital data demonstrated that the largest olivine spectral features (and inferred grain size) are found outside, and to the north, of Jezero (Brown et al., 2020). However, our findings for this regional lithology will remain uncertain until we are able to reach these locations for in situ observations. These occasions will no doubt be as informative as the visit of *Perseverance* to Séítah.

We have made the following new findings and interpretations:

1. We have used a Venn-diagrammatic approach to establish that the CRISM orbital datasets are not able to identify phyllosilicate features that have been mapped in situ with the SuperCam VISIR spectrometer, specifically with regards to their inability to map 2.38 and 2.46 μm bands (Figure 6).
2. Again using the Venn-diagrammatic approach, we have demonstrated the limited extent of alteration by phyllosilicate and carbonate, particularly for the Séítah subset of HRL000040FF. Figure 8 shows more than 50% of the olivine in this image is unaltered at orbital resolution.
3. As seen in Figure 6, there are regions of the CRISM HRL000040FF image that display the presence of all three olivine, phyllosilicate, and carbonate bands (known as the Margin Carbonates). However, there are regions where only phyllosilicates are present, with only a weak to vanishing 2.5 μm band. This is marked “Clay only” on the Figure 7 correlation plot.
4. Following previous work by Goudge et al. (2015) and Parente et al. (2021)

we have conducted a comparison of CRISM data inside Jezero crater to in situ VISIR observations and extended their interpretations to identify 6 different phyllosilicate types.

5. As seen in Figure 4 and 10, the IR spectra of phyllosilicates talc, lizardite, Mg/Fe smectite, hectorite, saponite and stevensite, are all broadly consistent with the spectra of Garde 207 and Dourbes Tailings 255. As seen in Figure 10, we have shown that talc is a potential match for the phyllosilicate signal in the VISIR spectra for Garde, and especially the Dourbes tailings, in accord with Mandon et al. (2023). We regard the suggestion of talc to be only plausible or tentative until the VISIR calibration is further improved (Royer et al., 2023), or more observations are made in locations of higher phyllosilicate abundance, for example in the Margin Carbonates region or potentially in the Noachian region outside of Jezero. Based on the lack of a strong 2.28 μm band, we can eliminate nontronite and hisingerite as the phyllosilicates in Garde and Dourbes.
6. Based on Table 3, showing the LIBS results for Cine/Garde and Ubraye/Dourbes, the low aluminum amounts for the olivine cumulate are not consistent with the presence of Al bearing phyllosilicates.
7. We propose that the olivine-phyllosilicate-carbonate lithology at the Séítah formation was emplaced as a ponded lava flow, with low viscosity, relatively deep flows, and lack of local low shield volcanoes.
8. We have presented a model suggesting that thermal-convection-driven cooling, balanced by crystallization of the lava, may have taken place in order to form large mm-sized crystals seen in the Séítah formation.
9. We have presented a model where olivine-rich lava ponded into a lava lake in Jezero crater, and then 40+/-10% of the magma in the lake crystallized. Based on RIMFAX data suggesting the Séítah formation was approximately 10m thick, this would lead to the bottom ~4m of the Séítah unit consisting of the Cine and Garde Bastide workspace olivine cumulate outcrop sampled by *Perseverance*. The original ponded lava body would necessarily have been thicker to allow differentiation of the olivine crystals and settling to the bottom of the chamber. This upper part would be more pyroxene than olivine-rich, as described in Wiens et al. (2022). It is likely that this portion of the ponded lava lake was removed prior to emplacement of later lava flows.
10. We have formulated a new conjecture that the olivine-rich lithology is the missing earlier, more voluminous ultramafic rocks proposed by Rampey and Harvey (2012). Needless to say, this will require further testing in situ.

6. Acknowledgements

This paper is dedicated to the memory of Hans Amundsen. We would like to thank Paolo Pilleri, Chip Legett and Dot DeLapp for their untiring work to keep the SuperCam tools and datasets up to date and ready for use in projects like this one. We thank Daniel Applin for measurement of the stevensite spectra. We would also like to thank François Poulet, Janice Bishop, Deanne Rogers and two anonymous reviewers, for helpful comments and suggestions on the manuscript. We also thank all of the people who contributed to the development and operations of the *Perseverance* rover. This work is supported by grants and contracts to the Mars 2020 project as part of the Mars Exploration Program.
AGF was supported by European Research Council, Consolidator Grant number 818602. JMM acknowledges funding from the Spanish Agency for Research AEI/MCIN/FEDER, grant PID2022-142750OB-I00.

Open Research

All CRISM and VISIR data used can be obtained from the Planetary Data System (PDS) Geoscience Node (Murchie, 2006 and Wiens and Maurice, 2021). All data and software used to produce the datasets in this manuscript are available at the Harvard Dataverse repistory for this paper (Brown, 2023).

7. References

Allwood, A.C., Wade, L.A., Foote, M.C., Elam, W.T., Hurowitz, J.A., Battel, S., Dawson, D.E., Denise, R.W., Ek, E.M., Gilbert, M.S., King, M.E., Liebe, C.C., Parker, T., Pedersen, D.A.K., Randall, D.P., Sharrow, R.F., Sondheim, M.E., Allen, G., Arnett, K., Au, M.H., Basset, C., Benn, M., Bousman, J.C., Braun, D., Calvet, R.J., Clark, B., Cinquini, L., Conaby, S., Conley, H.A., Davidoff, S., Delaney, J., Denver, T., Diaz, E., Doran, G.B., Ervin, J., Evans, M., Flannery, D.O., Gao, N., Gross, J., Grotzinger, J., Hannah, B., Harris, J.T., Harris, C.M., He, Y., Heirwegh, C.M., Hernandez, C., Hertzberg, E., Hodyss, R.P., Holden, J.R., Hummel, C., Jadusingh, M.A., Jørgensen, J.L., Kawamura, J.H., Kitiyakara, A., Kozaczek, K., Lambert, J.L., Lawson, P.R., Liu, Y., Luchik, T.S., Macneal, K.M., Madsen, S.N., McLennan, S.M., McNally, P., Meras, P.L., Muller, R.E., Napoli, J., Naylor, B.J., Nemere, P., Ponomarev, I., Perez, R.M., Pootrakul, N., Romero, R.A., Rosas, R., Sachs, J., Schaefer, R.T., Schein, M.E., Setterfield, T.P., Singh, V., Song, E., Soria, M.M., Stek, P.C., Tallarida, N.R., Thompson, D.R., Tice, M.M., Timmermann, L., Torossian, V., Treiman, A., Tsai, S., Uckert, K., Villalvazo, J., Wang, M., Wilson, D.W., Worel, S.C., Zamani, P., Zappe, M., Zhong, F., Zimmerman, R., 2020. PIXL: Planetary

Instrument for X-Ray Lithochemistry. Space Sci. Rev. 216, 134. https://doi.org/10.1007/s11214-020-00767-7

Alwmark, S., B. Horgan, A. Udry, A. Bechtold, S. Fagents, E. Ravanis, L. Crumpler, et al. “Diverse Lava Flow Morphologies in the Stratigraphy of the Jezero Crater Floor.” *Journal of Geophysical Research: Planets* 128, no. 7 (2023): e2022JE007446. https://doi.org/10.1029/2022JE007446.

Amelin, Y., Krot, A.N., Hutcheon, I.D., Ulyanov, A.A., 2002. Lead Isotopic Ages of Chondrules and Calcium-Aluminum-Rich Inclusions. Science 297, 1678–1683. https://doi.org/10.1126/science.1073950

Anderson, R.B., Forni, O., Cousin, A., Wiens, R.C., Clegg, S.M., Frydenvang, J., Gabriel, T.S.J., Ollila, A., Schröder, S., Beyssac, O., Gibbons, E., Vogt, D.S., Clavé, E., Manrique, J.-A., Legett, C., Pilleri, P., Newell, R.T., Sarrao, J., Maurice, S., Arana, G., Benzerara, K., Bernardi, P., Bernard, S., Bousquet, B., Brown, A.J., Alvarez-Llamas, C., Chide, B., Cloutis, E., Comellas, J., Connell, S., Dehouck, E., Delapp, D.M., Essunfeld, A., Fabre, C., Fouchet, T., Garcia-Florentino, C., García-Gómez, L., Gasda, P., Gasnault, O., Hausrath, E.M., Lanza, N.L., Laserna, J., Lasue, J., Lopez, G., Madariaga, J.M., Mandon, L., Mangold, N., Meslin, P.-Y., Nelson, A.E., Newsom, H., Reyes-Newell, A.L., Robinson, S., Rull, F., Sharma, S., Simon, J.I., Sobron, P., Fernandez, I.T., Udry, A., Venhaus, D., McLennan, S.M., Morris, R.V., Ehlmann, B., 2022. Post-landing major element quantification using SuperCam laser induced breakdown spectroscopy. Spectrochim. Acta Part B At. Spectrosc. 188, 106347. https://doi.org/10.1016/j.sab.2021.106347

Arndt, N.T., Lesher, C.M., Houlé, M.G., Lewin, E., Lacaze, Y., 2004. Intrusion and crystallization of a spinifex-textured komatiite sill in Dundonald Township, Ontario. J. Petrol. 45, 2555–2571.

Bailey, S.W., 1988. Hydrous phyllosilicates:(exclusive of micas). Walter de Gruyter GmbH & Co

Bartlett, Robert W. “Magma Convection, Temperature Distribution, and Differentiation.” *American Journal of Science* 267, no. 9 (1969): 1067–82.

Beyssac, O., O. Forni, A. Cousin, A. Udry, L. C. Kah, L. Mandon, O. E. Clavé, et al. “Petrological Traverse of the Olivine Cumulate Séítah Formation at Jezero Crater, Mars: A Perspective From SuperCam Onboard Perseverance.” *Journal of Geophysical Research: Planets* 128, no. 7 (2023): e2022JE007638. https://doi.org/10.1029/2022JE007638.

Bishop J. L., Noe Dobrea E. Z., McKeown N. K., Parente M., Ehlmann B. L., Michalski J. R., Milliken R. E., Poulet F., Swayze G. A., Mustard J. F., Murchie S. L. & Bibring J.-P. 2008a Phyllosilicate diversity and past aqueous activity revealed at Mawrth Vallis, Mars. Science, **321**, 830-833.

Bishop, J.L., Lane, M.D., Dyar, M.D., Brown, A.J., 2008b. Reflectance and emission spectroscopy of four groups of phyllosilicates: smectites, kaolinite-serpentines, chlorites and micas. Clay Miner. 43, 35–54.

Bishop, J.L., Perry, K.A., Darby Dyar, M., Bristow, T.F., Blake, D.F., Brown, A.J., Peel, S.E., 2013. Coordinated spectral and XRD analyses of magnesite-nontronite-forsterite mixtures and implications for carbonates on Mars. J. Geophys. Res. Planets 635–650.

Borg, L.E., Connelly, J.N., Nyquist, L.E., Shih, C.-Y., Wiesmann, H., Reese, Y., 1999. The age of the carbonates in Martian meteorite ALH84001. Science 286, 90–94.

Bottinga, Y., Weill, D.F., 1972. The viscosity of magmatic silicate liquids: A model for calculation. Am. J. Sci. 272, 438–475.

Brandeis, Geneviève, and Bruce D. Marsh. “The Convective Liquidus in a Solidifying Magma Chamber: A Fluid Dynamic Investigation.” *Nature* 339, no. 6226 (June 1989): 613–16. https://doi.org/10.1038/339613a0.

Brindley, G.W., Bish, D.L., Wan, H.-M., 1977. The nature of kerolite, its relation to talc and

stevensite. Mineral. Mag. 41, 443–452.
Brown, A. J., 2006a. Spectral Curve Fitting for Automatic Hyperspectral Data Analysis. IEEE Trans. Geosci. Remote Sens. 44, 1601–1608. https://doi.org/10.1109/TGRS.2006.870435
Brown, A.J., 2006b. Hyperspectral Mapping of Ancient Hydrothermal Systems (PhD). Macquarie University, Sydney, N.S.W.
Brown, Adrian, 2023, "Replication Data for: Properties of the Olivine-Clay-Carbonate lithology at Seitah",[Dataset] https://doi.org/10.7910/DVN/QEIVES, Harvard Dataverse, V3
Brown, A.J., Hook, S.J., Baldridge, A.M., Crowley, J.K., Bridges, N.T., Thomson, B.J., Marion, G.M., de Souza Filho, C.R., Bishop, J.L., 2010. Hydrothermal formation of Clay-Carbonate alteration assemblages in the Nili Fossae region of Mars. Earth Planet. Sci. Lett. 297, 174–182. https://doi.org/10.1016/j.epsl.2010.06.018
Brown, A.J., Viviano, C.E., Goudge, T.A., 2020. Olivine−Carbonate Mineralogy of the Jezero Crater Region. J. Geophys. Res. Planets 125, https://doi.org/10.1029/2019JE006011.
Brown, A.J., Walter, M.R., Cudahy, T.J., 2005. Hyperspectral Imaging Spectroscopy of a Mars Analog Environment at the North Pole Dome, Pilbara Craton, Western Australia. Aust. J. Earth Sci. 52, 353–364. https://doi.org/10.1080/08120090500134530
Chevrel, Magdalena Oryaëlle, Jérémie Labroquère, Andrew J. L. Harris, and Scott K. Rowland. “PyFLOWGO: An Open-Source Platform for Simulation of Channelized Lava Thermo-Rheological Properties.” *Computers & Geosciences* 111 (February 1, 2018): 167–80. https://doi.org/10.1016/j.cageo.2017.11.009.
Citron, R.I., Manga, M., Hemingway, D.J., 2018. Timing of oceans on Mars from shoreline deformation. Nature 555, 643–646. https://doi.org/10.1038/nature26144
Clark, R.N., Swayze, G.A., Wise, R., Livo, E., Hoefen, T., Kokaly, R., Sutley, S.J., 2007. USGS digital spectral library splib06a: http://speclab.cr.usgs.gov/spectral.lib06., Digital Data Series 231. U.S. Geological Survey.
Clavé, E., K. Benzerara, P.-Y. Meslin, O. Forni, C. Royer, L. Mandon, P. Beck, et al. “Carbonate Detection With SuperCam in Igneous Rocks on the Floor of Jezero Crater, Mars.” *Journal of Geophysical Research: Planets* 128, no. 6 (2023): e2022JE007463. https://doi.org/10.1029/2022JE007463.

Corpolongo, Andrea, Ryan S. Jakubek, Aaron S. Burton, Adrian J. Brown, Anastasia Yanchilina, Andrew D. Czaja, Andrew Steele, et al. “SHERLOC Raman Mineral Class Detections of the Mars 2020 Crater Floor Campaign.” *Journal of Geophysical Research: Planets* 128, no. 3 (2023): e2022JE007455. https://doi.org/10.1029/2022JE007455.

Crumpler, L. S., B. H. N. Horgan, J. I. Simon, K. M. Stack, S. Alwmark, G. Dromart, R. C. Wiens, et al. “In Situ Geologic Context Mapping Transect on the Floor of Jezero Crater From Mars 2020 Perseverance Rover Observations.” *Journal of Geophysical Research: Planets* 128, no. 10 (2023): e2022JE007444. https://doi.org/10.1029/2022JE007444.
Duke, E.F., 1994. Near infrared spectra of muscovite, Tschermak substitution, and metamorphic reaction progress: Implications for remote sensing. Geology 22, 621–624.
Edwards, Christopher S., and Bethany L. Ehlmann. “Carbon Sequestration on Mars.” *Geology* 43, no. 10 (August 21, 2015): G36983.1. https://doi.org/10.1130/G36983.1.
Ehlmann, B.L., Mustard, J.F., Murchie, S.L., Poulet, F., Bishop, J.L., Brown, A.J., Calvin, W.M., Clark, R.N., Marais, D.J.D., Milliken, R.E., Roach, L.H., Roush, T.L., Swayze, G.A., Wray, J.J., 2008. Orbital Identification of Carbonate-Bearing Rocks on Mars. Science 322, 1828–1832. https://doi.org/10.1126/science.1164759
Farley, K.A., Malespin, C., Mahaffy, P., Grotzinger, J.P., Vasconcelos, P.M., Milliken, R.E., Malin, M., Edgett, K.S., Pavlov, A.A., Hurowitz, J.A., Grant, J.A., Miller, H.B., Arvidson,

R., Beegle, L., Calef, F., Conrad, P.G., Dietrich, W.E., Eigenbrode, J., Gellert, R., Gupta, S., Hamilton, V., Hassler, D.M., Lewis, K.W., McLennan, S.M., Ming, D., Navarro-Gonz√°lez, R., Schwenzer, S.P., Steele, A., Stolper, E.M., Sumner, D.Y., Vaniman, D., Vasavada, A., Williford, K., Wimmer-Schweingruber, R.F., the, M.S.L.S.T., 2013. In Situ Radiometric and Exposure Age Dating of the Martian Surface. Science. https://doi.org/10.1126/science.1247166

Farley, K. A., K. M. Stack, D. L. Shuster, B. H. N. Horgan, J. A. Hurowitz, J. D. Tarnas, J. I. Simon, et al. “Aqueously Altered Igneous Rocks Sampled on the Floor of Jezero Crater, Mars.” *Science* 377, no. 6614 (August 25, 2022): eabo2196. https://doi.org/10.1126/science.abo2196.

Farley, K.A., Williford, K.H., Stack, K.M., Bhartia, R., Chen, A., de la Torre, M., Hand, K., Goreva, Y., Herd, C.D.K., Hueso, R., Liu, Y., Maki, J.N., Martinez, G., Moeller, R.C., Nelessen, A., Newman, C.E., Nunes, D., Ponce, A., Spanovich, N., Willis, P.A., Beegle, L.W., Bell, J.F., Brown, A.J., Hamran, S.-E., Hurowitz, J.A., Maurice, S., Paige, D.A., Rodriguez-Manfredi, J.A., Schulte, M., Wiens, R.C., 2020. Mars 2020 Mission Overview. Space Sci. Rev. 216, 142. https://doi.org/10.1007/s11214-020-00762-y

Fassett, Caleb I., and James W. Head. “Fluvial Sedimentary Deposits on Mars: Ancient Deltas in a Crater Lake in the Nili Fossae Region.” *Geophysical Research Letters* 32, no. 14 (July 28, 2005): L14201. https://doi.org/10.1029/2005GL023456.

García-Romero, E., Lorenzo, A., García-Vicente, A., Morales, J., García-Rivas, J., Suárez, M., 2021. On the structural formula of smectites: a review and new data on the influence of exchangeable cations. J. Appl. Crystallogr. 54, 251–262. https://doi.org/10.1107/S1600576720016040

Giordano, Daniele, James K. Russell, and Donald B. Dingwell. “Viscosity of Magmatic Liquids: A Model.” *Earth and Planetary Science Letters* 271, no. 1 (July 15, 2008): 123–34. https://doi.org/10.1016/j.epsl.2008.03.038.

Goudge, T.A., Mohrig, D., Cardenas, B.T., Hughes, C.M., Fassett, C.I., 2018. Stratigraphy and paleohydrology of delta channel deposits, Jezero crater, Mars. Icarus 301, 58–75.

Goudge, T.A., Mustard, J.F., Head, J.W., Fassett, C.I., Wiseman, S.M., 2015. Assessing the Mineralogy of the Watershed and Fan Deposits of the Jezero Crater Paleolake System, Mars. J. Geophys. Res. Planets 2014JE004782. https://doi.org/10.1002/2014JE004782

Grott, M., D. Baratoux, E. Hauber, V. Sautter, J. Mustard, O. Gasnault, S. W. Ruff, et al. “Long-Term Evolution of the Martian Crust-Mantle System.” *Space Science Reviews* 174, no. 1–4 (January 1, 2013): 49–111. https://doi.org/10.1007/s11214-012-9948-3.

Grosch, Eugene G., Janice L. Bishop, Christian Mielke, Alessandro Maturilli, and Jörn Helbert. “Early Archean Alteration Minerals in Mafic-Ultramafic Rocks of the Barberton Greenstone Belt as Petrological Analogs for Clay Mineralogy on Mars.” American Mineralogist 106, no. 5 (May 1, 2021): 672–84. https://doi.org/10.2138/am-2021-7656.

Guest, J. E., C. R. J. Kilburn, H. Pinkerton, and A. M. Duncan. “The Evolution of Lava Flow-Fields: Observations of the 1981 and 1983 Eruptions of Mount Etna, Sicily.” *Bulletin of Volcanology* 49, no. 3 (June 1, 1987): 527–40. https://doi.org/10.1007/BF01080447.

Hamilton, V.E., Christensen, P.R., 2005. Evidence for extensive, olivine-rich bedrock on Mars. Geology 33, 433–436.

Hamran, Svein-Erik, David A. Paige, Abigail Allwood, Hans E. F. Amundsen, Tor Berger, Sverre Brovoll, Lynn Carter, et al. “Ground Penetrating Radar Observations of Subsurface Structures in the Floor of Jezero Crater, Mars.” *Science Advances* 8, no. 34 (August 26, 2022): eabp8564. https://doi.org/10.1126/sciadv.abp8564.

Harris, Andrew J., and S. Rowland. “FLOWGO: A Kinematic Thermo-Rheological Model for Lava Flowing in a Channel.” *Bulletin of Volcanology* 63 (2001): 20–44.

Hiesinger, H., Head, J.W., 2004. The Syrtis Major volcanic province, Mars: Synthesis from Mars Global Surveyor data. J. Geophys. Res. 109, 10.1029/2003JE002143.
Hoefen, T.M., Clark, R.N., Bandfield, J.L., Smith, M.D., Pearl, J.C., Christensen, P.R., 2003. Discovery of Olivine in the Nili Fossae Region of Mars. Science 302, 627–630.
Horgan, B.H.N., Anderson, R.B., Dromart, G., Amador, E.S., Rice, M.S., 2020. The mineral diversity of Jezero crater: Evidence for possible lacustrine carbonates on Mars. Icarus 113526. https://doi.org/10.1016/j.icarus.2019.113526
Huppert, H.E., Sparks, R.S.J., 1985. Cooling and contamination of mafic and ultramafic magmas during ascent through continental crust. Earth Planet. Sci. Lett. 74, 371–386.
Huppert, H.E., Sparks, R.S.J., 1981. The fluid dynamics of a basaltic magma chamber replenished by influx of hot, dense ultrabasic magma. Contrib. Mineral. Petrol. 75, 279–289. https://doi.org/10.1007/BF01166768
Huppert, H.E., Sparks, R.S.J., Turner, J.S., Arndt, N.T., 1984. Emplacement and cooling of komatiite lavas. Nature 309, 13–16.
Isherwood, R.J., Jozwiak, L.M., Jansen, J.C., Andrews-Hanna, J.C., 2013. The volcanic history of Olympus Mons from paleo-topography and flexural modeling. Earth Planet. Sci. Lett. 363, 88–96.
Itoh Y. & Parente M. (2021) A new method for atmospheric correction and de-noising of CRISM hyperspectral data. Icarus, 354, 114024.
Jeffreys, Harold. “The Flow of Water in an Inclined Channel of Rectangular Section.” *The London, Edinburgh, and Dublin Philosophical Magazine and Journal of Science* 49, no. 293 (1925): 793–807. https://doi.org/10.1080/14786442508634662.
Kirkpatrick, R. James. “Kinetics of Crystal Growth in the System CaMgSi2O6 -CaAl2SiO6.” *American Journal of Science* 274, no. 3 (1974): 215–42. https://doi.org/10.2475/ajs.274.3.215.
Kremer, C.H., Mustard, J.F., Bramble, M.S., 2019. A widespread olivine-rich ash deposit on Mars. Geology. https://doi.org/10.1130/G45563.1
Lapen, T.J., Righter, M., Brandon, A.D., Debaille, V., Beard, B.L., Shafer, J.T., Peslier, A.H., 2010. A Younger Age for ALH84001 and Its Geochemical Link to Shergottite Sources in Mars. Science 328, 347–351.

Liu, Y., M. M. Tice, M. E. Schmidt, A. H. Treiman, T. V. Kizovski, J. A. Hurowitz, A. C. Allwood, et al. “An Olivine Cumulate Outcrop on the Floor of Jezero Crater, Mars.” *Science* 377, no. 6614 (September 30, 2022): 1513–19. https://doi.org/10.1126/science.abo2756.

Mandon, L., C. Quantin-Nataf, C. Royer, P. Beck, T. Fouchet, J. R. Johnson, E. Dehouck, et al. “Reflectance of Jezero Crater Floor: 2. Mineralogical Interpretation.” *Journal of Geophysical Research: Planets* n/a, no. n/a (2023): e2022JE007450. https://doi.org/10.1029/2022JE007450.
Mandon, L., Beck, P., Quantin-Nataf, C., Dehouck, E., Thollot, P., Loizeau, D., Volat, M., 2022. ROMA: A Database of Rock Reflectance Spectra for Martian In Situ Exploration. Earth Space Sci. 9, e2021EA001871. https://doi.org/10.1029/2021EA001871
Mandon, L., Quantin-Nataf, C., Thollot, P., Mangold, N., Lozac’h, L., Dromart, G., Beck, P., Dehouck, E., Breton, S., Millot, C., Volat, M., 2020. Refining the age, emplacement and alteration scenarios of the olivine-rich unit in the Nili Fossae region, Mars. Icarus 336, 113436. https://doi.org/10.1016/j.icarus.2019.113436
Mangold, N., Gupta, S., Gasnault, O., Dromart, G., Tarnas, J.D., Sholes, S.F., Horgan, B., Quantin-Nataf, C., Brown, A.J., Le Mouélic, S., 2021. Perseverance rover reveals an ancient delta-lake system and flood deposits at Jezero crater, Mars. Science eabl4051.

Mangold, N., D. Loizeau, F. Poulet, V. Ansan, D. Baratoux, S. LeMouelic, J. M. Bardintzeff, et al.

"Mineralogy of Recent Volcanic Plains in the Tharsis Region, Mars, and Implications for Platy-Ridged Flow Composition." *Earth and Planetary Science Letters*, Mars Express after 6 Years in Orbit: Mars Geology from Three-Dimensional Mapping by the High Resolution Stereo Camera (HRSC) Experiment, 294, no. 3 (June 1, 2010): 440–50. https://doi.org/10.1016/j.epsl.2009.07.036.

Mangold, N., Poulet, F., Mustard, J.F., Bibring, J.P., Gondet, B., Langevin, Y., Ansan, V., Masson, P., Fassett, C., Head, J.W., III, Hoffmann, H., Neukum, G., 2007. Mineralogy of the Nili Fossae region with OMEGA/Mars Express data: 2. Aqueous alteration of the crust. J. Geophys. Res. 112, doi:10.1029/2006JE002835.

Martin, P.E., Farley, K.A., Baker, M.B., Malespin, C.A., Schwenzer, S.P., Cohen, B.A., Mahaffy, P.R., McAdam, A.C., Ming, D.W., Vasconcelos, P.M., Navarro-González, R., 2017. A Two-Step K-Ar Experiment on Mars: Dating the Diagenetic Formation of Jarosite from Amazonian Groundwaters. J. Geophys. Res. Planets 122, 2803–2818. https://doi.org/10.1002/2017JE005445

Maurice, S., Wiens, R.C., Bernardi, P., Caïs, P., Robinson, S., Nelson, T., Gasnault, O., Reess, J.-M., Deleuze, M., Rull, F., 2021. The SuperCam instrument suite on the Mars 2020 rover: Science objectives and Mast-Unit description. Space Sci. Rev. 217, 1–108.

Murchie, S., Mars Reconnaissance Orbiter Compact Reconnaissance Imaging Spectrometer for Mars Multispectral Reduced Data Record, MRO-M-CRISM-5-RDR-MULTISPECTRAL-V1.0, doi:10.17189/1519437 NASA Planetary Data System, 2006.

Mustard, J.F., Poulet, F., Head, J.W., Mangold, N., Bibring, J.P., Pelkey, S.M., Fassett, C.I., Langevin, Y., Neukum, G., 2007. Mineralogy of the Nili Fossae region with OMEGA/Mars Express data: 1. Ancient impact melt in the Isidis Basin and implications for the transition from the Noachian to Hesperian. J. Geophys. Res. 112.

Nyquist, L.E., Shih, C.-Y., McCubbin, F.M., Santos, A.R., Shearer, C.K., Peng, Z.X., Burger, P.V., Agee, C.B., 2016. Rb-Sr and Sm-Nd isotopic and REE studies of igneous components in the bulk matrix domain of Martian breccia Northwest Africa 7034. Meteorit. Planet. Sci. 51, 483–498. https://doi.org/10.1111/maps.12606

Pinet, P., Chevrel, S., 1990. Spectral Identification of Geological Units on the Surface of Mars Related to the Presence of Silicates From Earth-Based Near-Infrared Telescopic Charge-Coupled Device Imaging. J. Geophys. Res. 95, 14435.

Parente, Mario, Arun M. Saranathan, Yuki Itoh, Jesse D. Tarnas, Frank P. Seelos, and John F. Mustard. "Map of the Dominant Mineralogy over and around the Mars2020 Landing Ellipse with Correspondent Spectral Signatures," October 14, 2021. https://doi.org/10.5281/zenodo.5575824.

Pinkerton, H., Wilson, L., 1994. Factors controlling the lengths of channel-fed lava flows. Bull. Volcanol. 56, 108–120. https://doi.org/10.1007/BF00304106

Plescia, J.B., 1990. Recent flood lavas in the Elysium region of Mars. Icarus 88, 465–490.

Poulet, F., Nicolas Mangold, B. Platevoet, J.-M. Bardintzeff, Violaine Sautter, John F. Mustard, J. P. Bibring, et al. "Quantitative Compositional Analysis of Martian Mafic Regions Using the MEx/OMEGA Reflectance Data: 2. Petrological Implications." *Icarus* 201, no. 1 (May 2009): 84–101. http://www.sciencedirect.com/science/article/B6WGF-4XH0MST-1/2/fb8c28702d9e37b8445c2e3b9fcbcd76.

Putirka, K., 2016. Rates and styles of planetary cooling on Earth, Moon, Mars, and Vesta, using new models for oxygen fugacity, ferric-ferrous ratios, olivine-liquid Fe-Mg exchange, and mantle potential temperature. Am. Mineral. 101, 819–840. https://doi.org/10.2138/am-2016-5402

Rampey, M., Harvey, R., 2012. Mars Hesperian Magmatism as Revealed by Syrtis Major and the Circum-Hellas Volcanic Province. Earth Moon Planets 109, 61–75.

https://doi.org/10.1007/s11038-012-9404-0

Robbins, S.J., Achille, G.D., Hynek, B.M., 2011. The volcanic history of Mars: High-resolution crater-based studies of the calderas of 20 volcanoes. Icarus 211, 1179–1203. https://doi.org/10.1016/j.icarus.2010.11.012

Rogers, D., Warner Nicholas H., Golombek Matthew P., Head James W., Cowart Justin C., 2018. Areally Extensive Surface Bedrock Exposures on Mars: Many Are Clastic Rocks, Not Lavas. Geophys. Res. Lett. 45, 1767–1777. https://doi.org/10.1002/2018GL077030

Roush, T.L., Bishop, J.L., Brown, A.J., Blake, D.F., Bristow, T.F., 2015. Laboratory reflectance spectra of clay minerals mixed with Mars analog materials: Toward enabling quantitative clay abundances from Mars spectra. Icarus 258, 454–466. https://doi.org/10.1016/j.icarus.2015.06.035

Rowland, Scott K., Andrew J. L. Harris, and Harold Garbeil. “Effects of Martian Conditions on Numerically Modeled, Cooling-Limited, Channelized Lava Flows.” *Journal of Geophysical Research: Planets* 109, no. E10 (2004). https://doi.org/10.1029/2004JE002288.

Royer, C., T. Fouchet, L. Mandon, F. Montmessin, F. Poulet, O. Forni, J. R. Johnson, et al. “Reflectance of Jezero Crater Floor: 1. Data Processing and Calibration of the Infrared Spectrometer (IRS) on SuperCam.” *Journal of Geophysical Research: Planets* 128, no. 1 (2023): e2022JE007481. https://doi.org/10.1029/2022JE007481.

Ruff, S.W., Hamilton, V.E., Rogers, A.D., Edwards, C.S., Horgan, B.H.N., 2022. Olivine and carbonate-rich bedrock in Gusev crater and the Nili Fossae region of Mars may be altered ignimbrite deposits. Icarus 380, 114974. https://doi.org/10.1016/j.icarus.2022.114974

Saranthan, A.M. and Parente, M (2021) Adversarial feature learning for improved mineral mapping of CRISM data. *Icarus* **355** 114107

Seelos, F. P., M. F. Morgan, H. W. Taylor, S. L. Murchie, D. C. Humm, K. D. Seelos, O. S. Barnouin, C. E. Viviano, and CRISM Team (2012), CRISM Map Projected Targeted Reduced Data Records (MTRDRs) – High Level Analysis and Visualization Data Products, in Planetary Data: A Workshop for Users and Software Developers, Flagstaff, AZ

Spera, Frank J. “Aspects of Magma Transport.” Edited by R. B. Hargraves. *Physics of Magmatic Processes* 7 (1980).

Sparks, R. S. J., H. Pinkerton, and R. Macdonald. “The Transport of Xenoliths in Magmas.” *Earth and Planetary Science Letters* 35, no. 2 (June 1, 1977): 234–38. https://doi.org/10.1016/0012-821X(77)90126-1.

Shahrzad, S., Kinch, K.M., Goudge, T.A., Fassett, C.I., Needham, D.H., Quantin−Nataf, C., Knudsen, C.P., 2019. Crater statistics on the dark-toned, mafic floor unit in Jezero Crater, Mars. Geophys. Res. Lett. 0. https://doi.org/10.1029/2018GL081402

Shaw, Herbert R. “Comments on Viscosity, Crystal Settling, and Convection in Granitic Magmas.” *American Journal of Science* 263, no. 2 (1965): 120–52.

Sholes, S.F., Dickeson, Z.I., Montgomery, D.R., Catling, D.C., 2021. Where are Mars’ hypothesized ocean shorelines? Large lateral and topographic offsets between different versions of paleoshoreline maps. J. Geophys. Res. Planets 126, e2020JE006486.

Sholes, S.F., Rivera-Hernández, F., 2022. Constraints on the uncertainty, timing, and magnitude of potential Mars oceans from topographic deformation models. Icarus 378, 114934.

Simon, J. I., K. Hickman-Lewis, B. A. Cohen, L.E. Mayhew, D.L. Shuster, V. Debaille, E. M.

Hausrath, et al. “Samples Collected from the Floor of Jezero Crater with the Mars 2020 Perseverance Rover.” *Journal of Geophysical Research: Planets* 128, no. 6 (2023). https://doi.org/10.1029/2022JE007474.

Stack, K.M., Williams, N.R., Calef, F., Sun, V.Z., Williford, K.H., Farley, K.A., Eide, S., Flannery, D., Hughes, C., Jacob, S.R., Kah, L.C., Meyen, F., Molina, A., Nataf, C.Q., Rice, M., Russell, P., Scheller, E., Seeger, C.H., Abbey, W.J., Adler, J.B., Amundsen, H., Anderson, R.B., Angel, S.M., Arana, G., Atkins, J., Barrington, M., Berger, T., Borden, R., Boring, B., Brown, A., Carrier, B.L., Conrad, P., Dypvik, H., Fagents, S.A., Gallegos, Z.E., Garczynski, B., Golder, K., Gomez, F., Goreva, Y., Gupta, S., Hamran, S.-E., Hicks, T., Hinterman, E.D., Horgan, B.N., Hurowitz, J., Johnson, J.R., Lasue, J., Kronyak, R.E., Liu, Y., Madariaga, J.M., Mangold, N., McClean, J., Miklusicak, N., Nunes, D., Rojas, C., Runyon, K., Schmitz, N., Scudder, N., Shaver, E., SooHoo, J., Spaulding, R., Stanish, E., Tamppari, L.K., Tice, M.M., Turenne, N., Willis, P.A., Aileen Yingst, R., 2020. Photogeologic Map of the Perseverance Rover Field Site in Jezero Crater Constructed by the Mars 2020 Science Team. Space Sci. Rev. 216, 127. https://doi.org/10.1007/s11214-020-00739-x

Sun, Vivian Z., Kevin P. Hand, Kathryn M. Stack, Ken A. Farley, Justin I. Simon, Claire Newman, Sunanda Sharma, et al. “Overview and Results From the Mars 2020 Perseverance Rover’s First Science Campaign on the Jezero Crater Floor.” *Journal of Geophysical Research: Planets* 128, no. 6 (2023): e2022JE007613. https://doi.org/10.1029/2022JE007613.

Tarnas, J.D., Stack, K.M., Parente, M., Koeppel, A.H.D., Mustard, J.F., Moore, K.R., Horgan, B.H.N., Seelos, F.P., Cloutis, E.A., Kelemen, P.B., Flannery, D., Brown, A.J., Frizzell, K.R., Pinet, P., 2021. Characteristics, Origins, and Biosignature Preservation Potential of Carbonate-Bearing Rocks Within and Outside of Jezero Crater. J. Geophys. Res. Planets 126, e2021JE006898. https://doi.org/10.1029/2021JE006898

Tice, Michael M., Joel A. Hurowitz, Abigail C. Allwood, Michael W. M. Jones, Brendan J. Orenstein, Scott Davidoff, Austin P. Wright, et al. “Alteration History of Séítah Formation Rocks Inferred by PIXL X-Ray Fluorescence, x-Ray Diffraction, and Multispectral Imaging on Mars.” *Science Advances* 8, no. 47 (November 25, 2022): eabp9084. https://doi.org/10.1126/sciadv.abp9084.

Tornabene, L.L., Moersch, J.E., McSween, H.Y., Hamilton, V.E., Piatek, J.L., Christensen, P.R., 2008. Surface and crater-exposed lithologic units of the Isidis Basin as mapped by coanalysis of THEMIS and TES derived data products. J. Geophys. Res. Planets 113, E10001. https://doi.org/10.1029/2007JE002988

Treiman, A.H., 2005. The nakhlite meteorites: Augite-rich igneous rocks from Mars. Geochemistry 65, 203–270. https://doi.org/10.1016/j.chemer.2005.01.004

Treiman, A.H., Morris, R.V., Agresti, D.G., Graff, T.G., Achilles, C.N., Rampe, E.B., Bristow, T.F., Ming, D.W., Blake, D.F., Vaniman, D.T., Bish, D.L., Chipera, S.J., Morrison, S.M., Downs, R.T., 2014. Ferrian saponite from the Santa Monica Mountains (California, U.S.A., Earth): Characterization as an analog for clay minerals on Mars with application to Yellowknife Bay in Gale Crater. Am. Mineral. 99, 2234–2250. https://doi.org/10.2138/am-2014-4763

Turenne, Nathalie, Sahejpal Sidhu, Daniel M. Applin, Edward A. Cloutis, Z. U. Wolf, Stanley A. Mertzman, Elisabeth M. Hausrath, Teresa Fornaro, and Adrian Brown. “Spectral Reflectance Properties of Nontronite Exposed to Mars-like Surface Conditions and Low-Temperature Heating (< 300° C).” *Icarus*, 2023, 115448.

Udry, A., A. Ostwald, V. Sautter, A. Cousin, O. Beyssac, O. Forni, G. Dromart, et al. “A Mars 2020 Perseverance SuperCam Perspective on the Igneous Nature of the Máaz Formation at Jezero Crater and Link With Séítah, Mars.” *Journal of Geophysical Research: Planets* 128, no. 7 (2023): e2022JE007440. https://doi.org/10.1029/2022JE007440.

Van Kranendonk, M. J., Hickman, A. H., Smithies, R. H., Nelson, D. R. and Pike, G. (2002) Geology and tectonic evolution of the archean North Pilbara terrain, Pilbara Craton, Western Australia. *Economic Geology and the Bulletin of the Society of Economic Geologists*, 97 (4), 695-732.

Vaucher, J., D. Baratoux, M. J. Toplis, P. Pinet, N. Mangold, and K. Kurita. “The Morphologies of Volcanic Landforms at Central Elysium Planitia: Evidence for Recent and Fluid Lavas on Mars.” *Icarus* 200, no. 1 (March 1, 2009): 39–51. https://doi.org/10.1016/j.icarus.2008.11.005.

Werner, S.C., 2008. The early martian evolution—Constraints from basin formation ages. Icarus 195, 45–60. https://doi.org/10.1016/j.icarus.2007.12.008

Wichman, R.W., Schultz, P.H., 1989. Sequence and mechanisms of deformation around the Hellas and Isidis Impact Basins on Mars. J. Geophys. Res. Solid Earth 94, 17333–17357. https://doi.org/10.1029/JB094iB12p17333

Wiens, Roger C., Arya Udry, Olivier Beyssac, Cathy Quantin-Nataf, Nicolas Mangold, Agnès Cousin, Lucia Mandon, et al. “Compositionally and Density Stratified Igneous Terrain in Jezero Crater, Mars.” *Science Advances* 8, no. 34 (August 25, 2022): eabo3399. https://doi.org/10.1126/sciadv.abo3399.

Wiens, Roger C. and Maurice, Sylvestre A. Mars 2020 Perseverance Rover SuperCam Raw, Calibrated, and Derived Data Products, doi:10.17189/1522646 NASA Planetary Data System, 2021.

Wiens, R.C., Maurice, S., Robinson, S.H., Nelson, A.E., Cais, P., Bernardi, P., Newell, R.T., Clegg, S., Sharma, S.K., Storms, S., 2021. The SuperCam instrument suite on the NASA Mars 2020 rover: Body unit and combined system tests. Space Sci. Rev. 217, 1–87.

Williford, K.H., Farley, K.A., Stack, K.M., Allwood, A.C., Beaty, D., Beegle, L.W., Bhartia, R., Brown, A.J., de la Torre Juarez, M., Hamran, S.-E., Hecht, M.H., Hurowitz, J.A., Rodriguez-Manfredi, J.A., Maurice, S., Milkovich, S., Wiens, R.C., 2018. Chapter 11 - The NASA Mars 2020 Rover Mission and the Search for Extraterrestrial Life, in: Cabrol, N.A., Grin, E.A. (Eds.), From Habitability to Life on Mars. Elsevier, pp. 275–308. https://doi.org/10.1016/B978-0-12-809935-3.00010-4

Wilson, L., Head, J.W., 1994. Mars - Review and Analysis of Volcanic-Eruption Theory and Relationships to Observed Landforms. Rev. Geophys. 32, 221–263.

Worster, M.Grae, Herbert E. Huppert, and R. Stephen J. Sparks. “Convection and Crystallization in Magma Cooled from Above.” *Earth and Planetary Science Letters* 101, no. 1 (1990): 78–89. https://doi.org/10.1016/0012-821X(90)90126-I.

Worster, M.G., Huppert, H.E., Sparks, R.S.J., 1993. The crystallization of lava lakes. J. Geophys. Res. Solid Earth 98, 15891–15901. https://doi.org/10.1029/93JB01428

Zastrow, A.M., Glotch, T.D., 2021. Distinct carbonate lithologies in Jezero crater, Mars. Geophys. Res. Lett. 48, e2020GL092365.

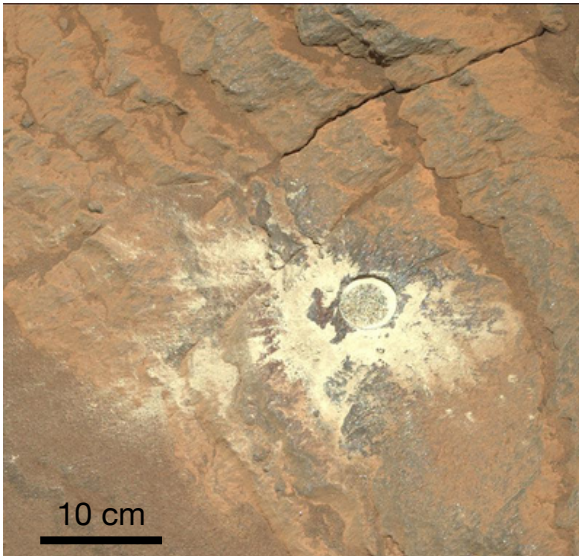
10 cm

a

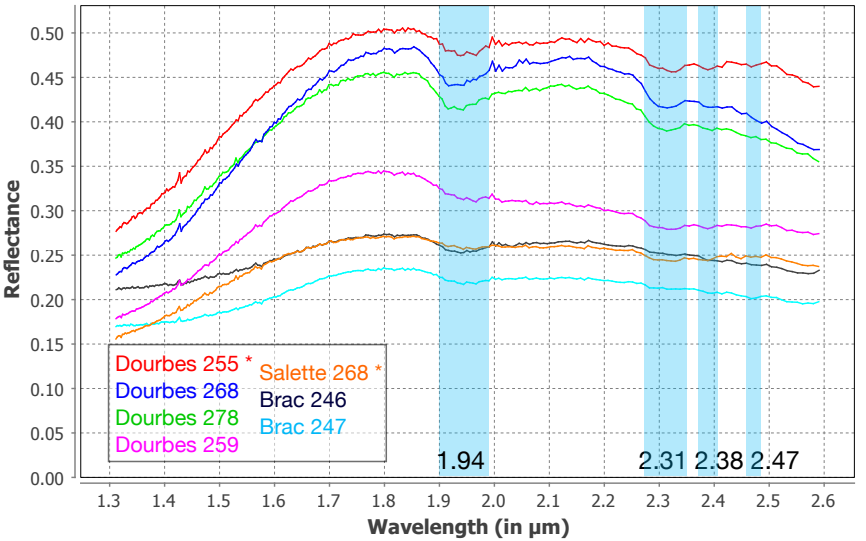
Reflectance
0.50
0.45
0.40
0.35
0.30
0.25
0.20
0.15
0.10
0.05
0.00
1.3
1.4
1.5
1.6
1.7
1.8
1.9
2.0
2.1
2.2
2.3
2.4
2.5
2.6
Wavelength (in µm)
Dourbes 255 *
Salette 268 *
Dourbes 268
Brac 246
Dourbes 278
Brac 247
Dourbes 259
1.94
2.31
2.38
2.47

b

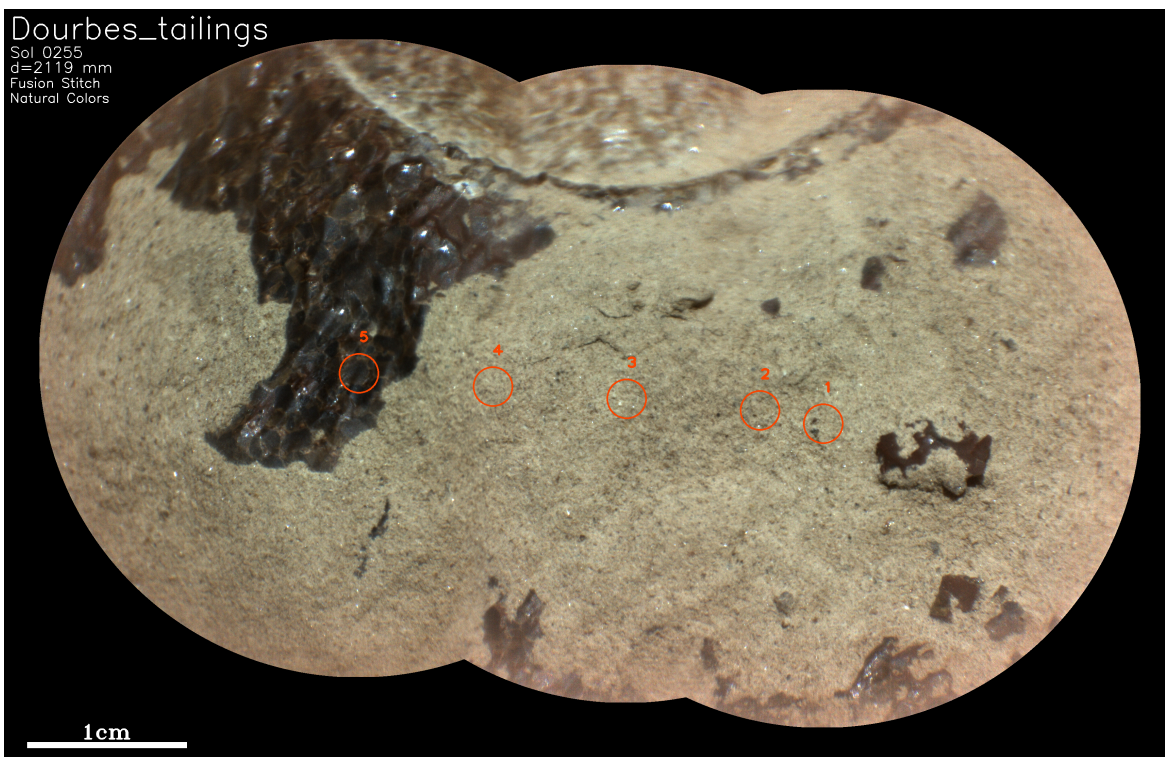
Dourbes_tailings
Sol 0255
d=2119 mm
Fusion Stitch
Natural Colors
5
4
3
2
1
1cm

c

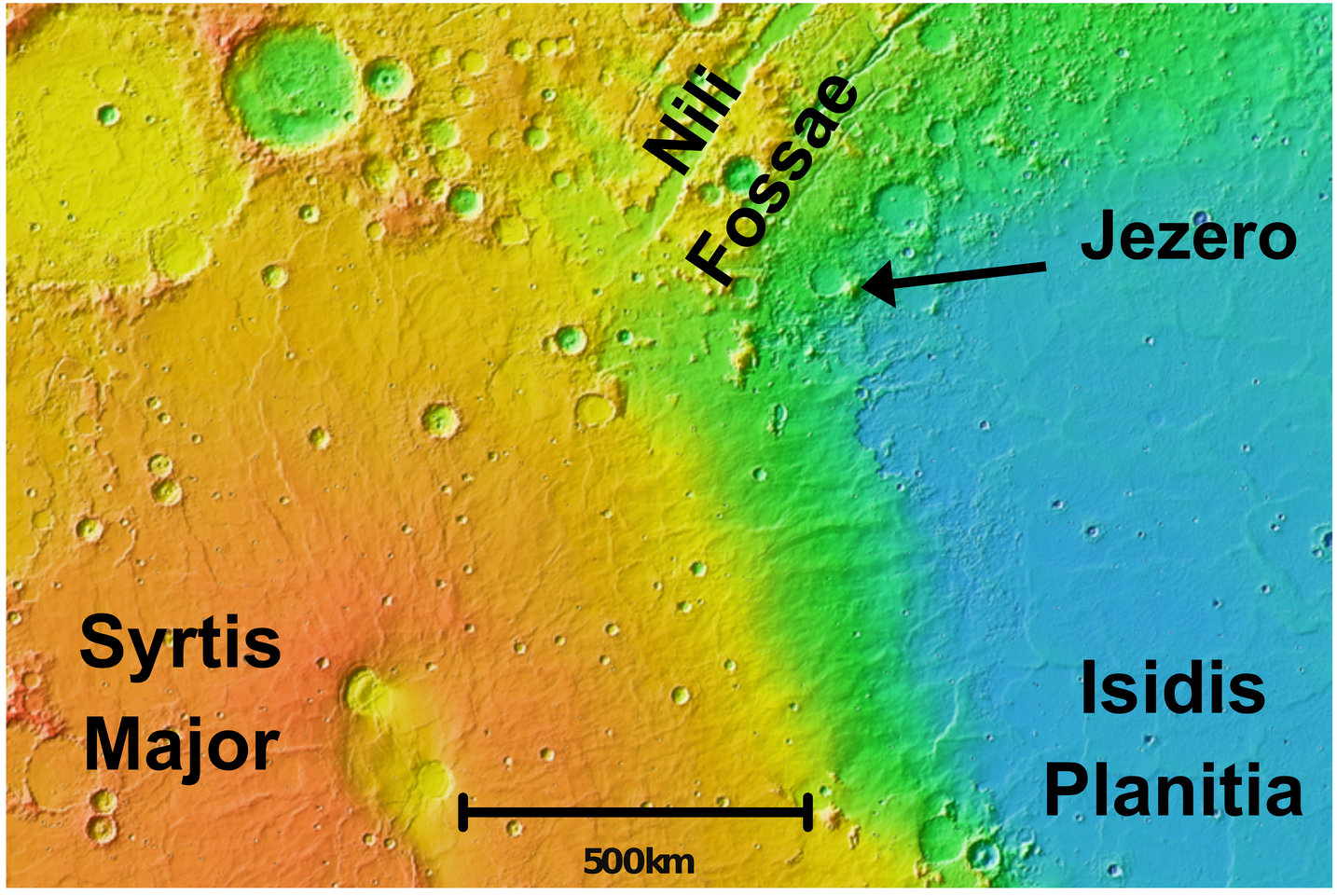
Nili
Fossae
Jezero
Syrtis
Major
Isidis
Planitia
500km

a

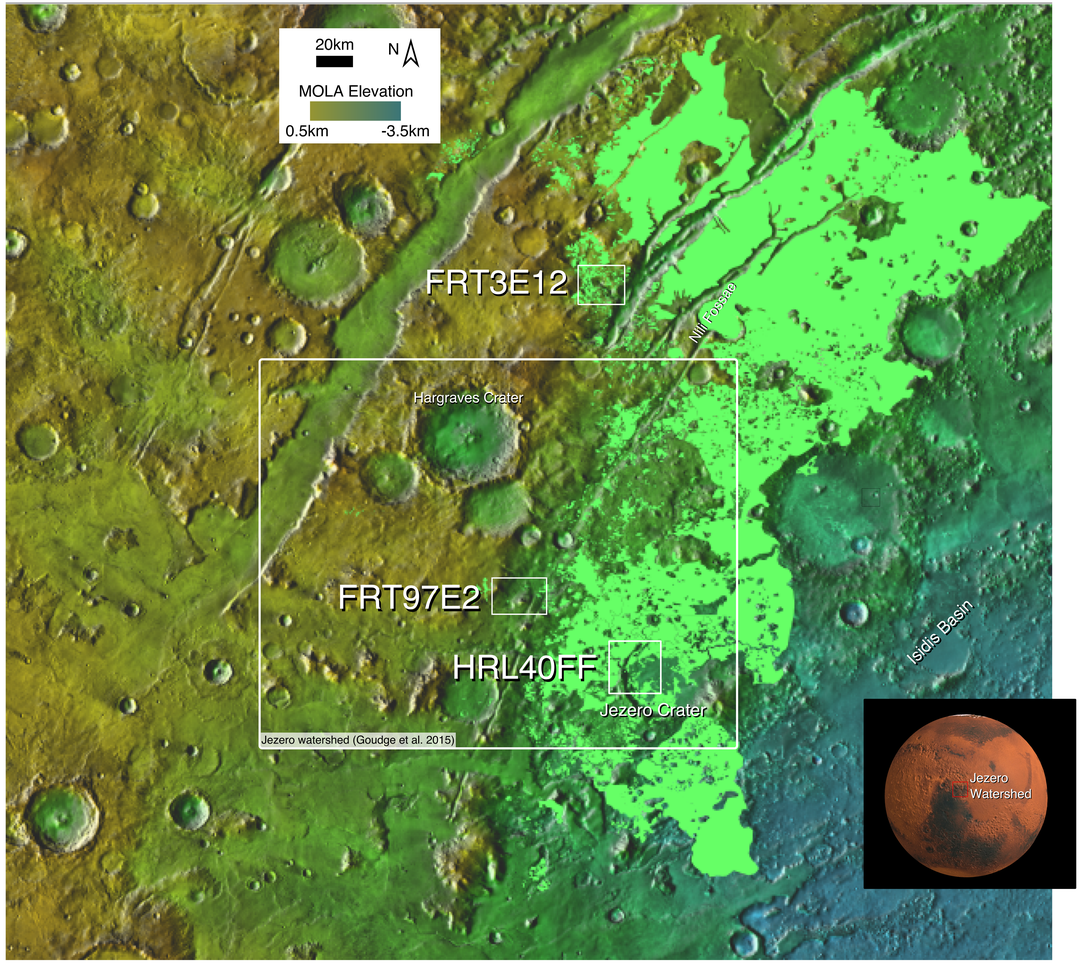
20km
N
MOLA Elevation
0.5km
-3.5km
FRT3E12
Nili Fossae
Hargraves Crater
FRT97E2
HRL40FF
Jezero Crater
Isidis Basin
Jezero watershed (Goudge et al. 2015)
Jezero
Watershed

b

Journal of Geophysical Research

Supporting Information for

Properties of the Nili Fossae Olivine-rich lithology: orbital and in situ at Séítah

Adrian J. Brown*[1], Linda Kah[2] , Lucia Mandon[3], Roger Wiens[4], Patrick Pinet[5], Elise Clavé[6], Stéphane Le Mouélic[7], Arya Udry[8], Patrick J. Gasda[9], Clément Royer[10], Keyron Hickman-Lewis[11], Agnes Cousin[12], Justin I. Simon[13], Jade Comellas[14], Edward Cloutis[15], Thierry Fouchet[16], Alberto G. Fairén[17], Stephanie Connell[15], David Flannery[18], Briony Horgan[4], Lisa Mayhew[19], Allan Treiman[20], Jorge I. Núñez[21], Brittan Wogsland[2], Karim Benzerara[22], Hans E.F. Amundsen[23], Cathy Quantin-Nataf[24], Kevin P. Hand[25], Vinciane Debaille[26], Ari Essunfeld[9], Pierre Beck[27], Nicholas J. Tosca[28], Juan M. Madariaga[29], and Olivier Forni[12]

[1]Plancius Research, Severna Park, MD 21146. [2]Department of Earth and Planetary Sciences, University of Tennessee, Knoxville TN 37996, [3]LESIA, Observatoire de Paris, Université PSL, CNRS, Sorbonne Université, Université de Paris, Meudon, France, [4]Earth, Atmospheric, and Planetary Sciences, Purdue University, [5]IRAP, Observatoire Midi-Pyrénées,CNRS, Toulouse university, France, [6]CELIA, Université de Bordeaux, CNRS, CEA, [7]Laboratoire Planétologie et Géosciences, CNRS UMR 6112, Nantes Université, Université Angers, 44322 Nantes, France, [8]Department of Geoscience, University of Nevada Las Vegas, 89154 Las Vegas, NV, [9]Los Alamos National Laboratory, PO Box 1663 Los Alamos, NM 87545, [10]LESIA, Observatoire de Paris, Université PSL, CNRS, Sorbonne Université, Université de Paris, Meudon, France, [11]The Natural History Museum, Cromwell Road, London, SW7 5BD, UK, [12]IRAP, Observatoire Midi-Pyrénées, CNRS, Toulouse university, France, [13]Center for Isotope Cosmochemistry and Geochronology, Astromaterials Research & Exploration Science Division, NASA Johnson Space Center, 2101 Nasa Parkway, Houston, TX, 77058 USA, [14]University of Hawai'i at Mānoa, [15]University of Winnipeg, Canada, [16]LESIA, Observatoire de Paris, Université PSL, CNRS, Sorbonne Université, Université de Paris, Meudon, France, [17]Centro de Astrobiologia (CSIC-INTA) & Cornell University, NY, [18]Queensland University of Technology, Queensland, Australia, [19]Department of Geological Sciences, University of Colorado Boulder, Boulder, CO 80309, [20]Lunar and Planetary Institute, Houston TX 77058, [21]Johns Hopkins University Applied Physics Laboratory, Laurel, MD 20723, [22]Institut de Minéralogie, Physique des Matériaux et Cosmochimie, CNRS, Museum National d'Histoire Naturelle, Sorbonne Université, Paris, France, [23]Deceased, [24]University of Lyon, France, [25]Jet Propulsion Laboratory, Pasadena, CA 91109, [26]Laboratoire G-Time, Université libre de Bruxelles, Brussels, Belgium, [27]Institut de Planétologie et d'Astrophysique de Grenoble IPAG/CNRS, Université Grenoble Alpes, 414 rue de la piscine, 38041 Grenoble cedex 09, France, [28]Department of Earth Sciences, University of Cambridge, Downing Street, Cambridge, CB2 3EQ, United Kingdom, [29]Department of Analytical Chemistry, University of the Basque Country UPV/EHU, 48940 Leioa, Spain

S1 - Image identifiers

The following Table provides the Mars 2020 image IDs for Figures in the paper.

Fig.	Instrument	Sol	Image ID
1c	NavCam	248	NLF_0248_0688961170_442ECM_N0080000NCAM02248_07_195J
1d	ZCam	333	QZCAM_SOL0333_ZCAM08355_L0_Z110_ISSOLE_WORKSPACE_VP_4X_E01
11a	ZCam	340	ZR0_0255_0689576242_738EBY_N0080000ZCAM08278_0340LMJ

S2 - Sample provenance

The samples that were used to obtain the spectra in Figure 4 and 10 have various provenances. The talc and lizardite spectra are from the USGS Spectral library. The Fe/Mg smectite, hectorite and saponite spectra were supplied by Janice Bishop. Hectorite SHCa-1 (JB0172, <2 μm) and saponite SapCa-1 (JB1184c, 125-150 μm) were obtained from the Clay Minerals Source Clays Repository and the Fe/Mg smectite sample (JB0761a, <125 μm) was collected by J. Post from Flagstaff Hill, CA. Spectra of the hectorite and Fe/Mg smectite samples are described in Bishop et al. (2008a), while the saponite spectra are described in Roush et al. (2015).

The stevensite sample was supplied by Nicholas Tosca. The spectra of the sample were obtained by Ed Cloutis and Dan Applin at the University of Winnipeg. It was sourced from carbonate-rich sediments sampled from saline deposits of the Amargosa Desert, Nevada, USA. The following notes were taken on collection:

Aliquots were hand crushed in an agate mortar and pestle in order to increase surface area and increase the effectiveness of the carbonate dissolution step. Once crushed, powders were added to stirring beakers of 3 mol/kg acetic acid. During this step, pH was carefully monitored during carbonate dissolution in order to ensure the pH did not drop below levels which encourage the rapid dissolution of Mg-rich clays (Moore & Reynolds, 1997). Carbonate dissolution was taken to reach completion when the pH remained static for several hours after the addition of excess acid. At this stage, samples were centrifuged repeatedly with deionised water until the pH of the rinse reached ~6. A small amount of sodium phosphate salt was added to each clay suspension which buffers pH at ~7 and encourages the separation of clay mineral crystals in solution. Samples were then treated in an ultrasonic bath for 10 minutes to encourage separation of individual crystallites and centrifuged to remove the <2μm fraction. Oriented aggregate specimens of the <2μm fraction were prepared by vacuum filtration and deposition of an oriented clay film on a glass slide (Moore & Reynolds, 1997). This method of sample preparation is known to be the most representative of relative clay mineral abundances and results in little to no size fractionation effects (Moore & Reynolds, 1997).

For X-ray diffraction analysis, samples were analyzed on a Panalytical Empyrean powder X-ray diffractometer. Clay mineral specimens were analyzed after three different treatments: (1) in the air-dried state, (2) after exposure to ethylene glycol vapor for 14 days (as the kinetics of Mg-rich clay

mineral ethylene glycol solvation are known to be slow), and (3) after heating to 500°C and re-solvation with ethylene glycol vapor. These combined treatments allow the identification of smectite, kaolinite, chlorite, illite and other clay mineral sub-groups, but additional analyses are required to confirm the speciation of clay minerals (e.g., distinguishing the smectite-group minerals: stevensite, saponite and montmorillonite). In addition to powder X-ray diffraction, samples were also prepared for FT-IR analysis as discussed above.

References:

Khoury, H. N., Eberl, D. D. & Jones, B. F. Origin of Magnesium Clays from the Amargosa Desert, Nevada. Clay Clay Miner 30, 327–336 (1982).

Moore, D.M., and R.C. Reynolds Jr. X-Ray Diffraction and the Identification and Analysis of Clay Minerals. 2nd ed., 1997.

S3 – CRISM comparison assessment

As part of this project, we have conducted a comparison to an earlier CRISM study of Parente et al. (2021), which is available at the Zenodo web archive. We believe this comparison is able to give greater context to our work, since the Parente study contained a mineral map of the HRL000040FF CRISM image, that we present in Figure S.1.a. The Parente study also provided endmember spectra for the 10 type minerals they identified, these are shown in Figure S.1.b.

This analysis allows us to emphasize that the low Al phyllosilicate mineral findings we have reported in this study are restricted to the Séítah formation, and in fact high Al phyllosilicates are also in abundance in Jezero crater.

As for the correlation maps in our Figure 7, we obtained the endmember spectra from the Zenodo site and performed an Asymmetric Gaussian fit on the 1.0, 2.31, 2.38 and 2.5 μm bands, with shoulders at 1.012,1.75;2.25, 2.37; 2.37, 2.39; 2.425, 2.575. The band fitting results for the 1 and 2.31 μm for the 10 endmember spectra are shown in Figure S.2c. The band depths are relatively low compared with Spectral Library spectra, and have been averaged in 5x5 regions by the Parente study.

Figure S.1c shows that the Mg-carbonate is both rich in olivine and in carbonate, which is in keeping with olivine occurring with carbonate (e.g. Goudge et al 2015). The opal-carbonate is also shown as relatively olivine rich, and the Fe-olivine is olivine rich and carbonate poor. The pyroxene spectra had relatively low 2.31 and 1 μm bands.

The Mg-smectite (new) spectrum is interesting because it has relatively low olivine signature, and shows it has a 2.31 μm band associated with the Mg-OH band, which overlaps with the Mg-carbonate band. The 2.5 CRISM bands are very weak and so we have decided not to use them in this figure.

This comparison provides another link to previous work in the literature. In addition to the Parente study, Goudge et al. (2015) also studied the CRISM spectra in the region, and also found smectites in the HRL000040FF image.

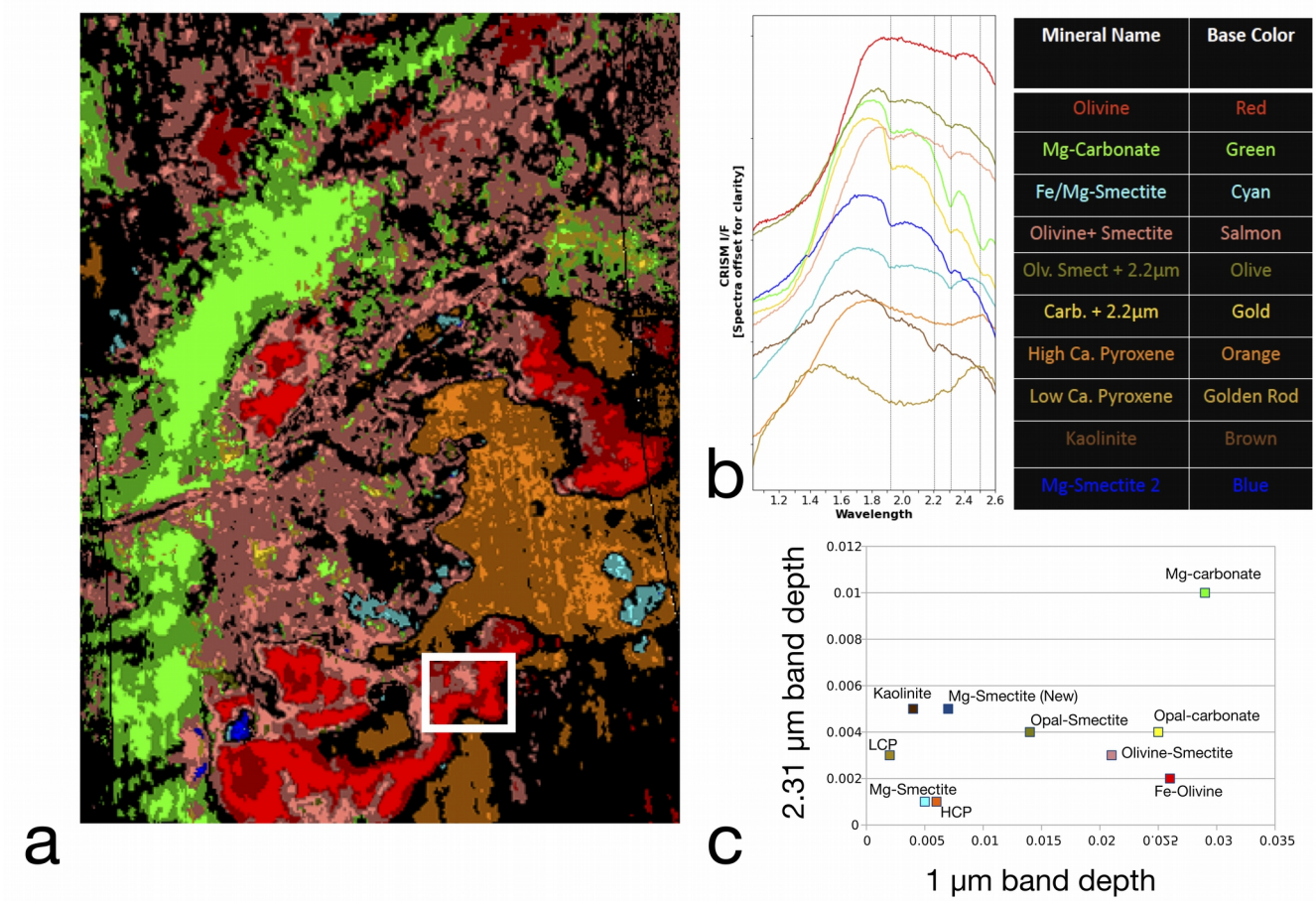

Figure S.1: A) Location of study site compared to Parente et al. (2021) mineral map of nearby regions of CRISM image HRL000040FF. White box shows Séítah subset studied in Figure 9. B) Spectra of mineral endmembers found in HRL000040FF (Parente et al., 2021). C) Band fitting results for endmember spectra.

References:

Goudge, Timothy A., John F. Mustard, James W. Head, Caleb I. Fassett, and Sandra M. Wiseman. "Assessing the Mineralogy of the Watershed and Fan Deposits of the Jezero Crater Paleolake System, Mars: Jezero Paleolake System Mineralogy." Journal of Geophysical Research: Planets 120, no. 4 (2015): 775–808. https://doi.org/10.1002/2014JE004782.

Parente, Mario, Arun M. Saranathan, Yuki Itoh, Jesse D. Tarnas, Frank P. Seelos, and John F. Mustard. "Map of the Dominant Mineralogy over and around the Mars2020 Landing Ellipse with Correspondent Spectral Signatures," (2021). https://doi.org/10.5281/zenodo.5575824.

S4 - LIBS accuracy assessment

We used a Monte Carlo bootstrapping technique to randomly draw values from the distribution defined by the accuracy and precision of each oxide in the composition of an observation point. For example, for an observation point with a composition of 44.2 wt% SiO2 +/- 6.1 wt%, we construct a normal distribution centered at 44.2 with standard deviation 6.1 and sample from this to simulate other possible SiO_2 values. If using precision, rather than accuracy, the normal distribution is still centered at the nominal value (e.g., 44.2 wt%), but the standard deviation used for the simulated distribution is generally lower, (e.g., 1.6 wt%, rather than 6.1 wt%; Anderson et al., 2021). We then convert these simulated oxide values (wt%) values to molar proportions, add them as indicated on the figure, renormalize the data (the standard procedure for plotting on ternary diagrams), and plot this cloud of points on the ternary diagram around the anchor composition. Using these three distributions and their standard deviations, we can calculate the standard deviation of these normalized molar distributions. The area of the inner polygon represents 1-sigma and the outer polygon represents 2-sigma. Hence, these plots can visualize and test for statistical separation of any two types of composition on a ternary plot or help to determine whether a composition is consistent with any type of endmember composition (i.e., the chemistry of one of the SuperCam calibration targets).

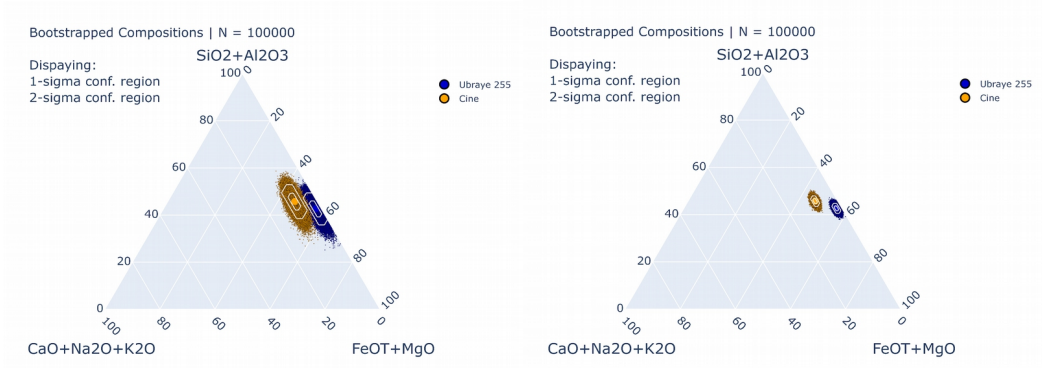

Figure S.2: The Monte Carlo simulated compositions (left: using instrument accuracy; right: using instrument precision) of target Y and Z using the average of all observation points, with N=10^5 simulation points for each target, on a SA CNK FM ternary diagram. The 1- and 2-sigma contours are drawn with white lines on the plot.